Vulnerability of power distribution utility poles to tsunami bore impacts

Max Taylor Stephens[1], Zhonghou Xu[2], Colin Whittaker[1], and Liam Wotherspoon[1]

Abstract

Recent events have demonstrated that power distribution networks located in low-lying coastal areas are susceptible to damage from tsunami. Utility poles are a critical component of distribution networks as they support overhead power lines. Damage to the poles could therefore compromise the electricity supply to emergency facilities as well as to homes and businesses over large areas. This work quantifies the component-level tsunami vulnerability of common power distribution line utility poles, considering hydrodynamic wave-impact loading effects but neglecting debris impact and scour effects. First, a series of scaled flume experiments were used to identify the relationship between the tsunami wave properties and hydrodynamic loading histories. Next, nonlinear numerical distribution line utility pole models were validated using the experimental data and extended to account for soil-structure interaction effects. Finally, the loading histories from the flume tests were scaled and used in the numerical models to perform an incremental dynamic tsunami analysis on varying pole geometries and loading orientations at prototype scale. The results from this work provide valuable insight into the response of power distribution poles subjected to tsunami attack. This includes validating idealised approaches to determine the expected failure mode(s) based on pole embedment depths and soil properties and providing probabilistic tools capable of estimating damage based on expected tsunami inundation depths.

Keywords:

[1]max.stephens@auckland.ac.nz,
c.whittaker@auckland.ac.nz,
l.wotherspoon@auckland.ac.nz; University of Auckland, Auckland, New Zealand
[2]zhonghou.xu@niwa.co.nz; National Institute of Water and Atmospheric Research NIWA, Hamilton, New Zealand

1 Introduction

Surveys of affected areas following the 2004 Indian Ocean Tsunami and the 2011 Tohoku Earthquake and Tsunami revealed widespread damage to a large variety of coastal infrastructure (Fritz et al., 2012; Mori and Takahashi, 2012; Shimozono et al., 2012; Ewing et al., 2013; Foytong et al., 2013; Fraser et al., 2013; Kawashima and Buckle, 2013). This widespread damage has renewed concern regarding the potential for future tsunamis to generate similar impacts in other locations. Many nations located on the Pacific Ring of Fire are exposed to tsunamis from both local and distant sources (De Lange and Healy, 2001; Power et al., 2012). Much of

the population in this part of the world resides in cities and towns along the coastline, such that any tsunami reaching the coastline could potentially affect a large proportion of the total population (De Lange and Healy, 1986); evidence for such events is found in the paleotsunami record in New Zealand (Goff et al., 2010, 2018). These impacts can be exacerbated by damage to critical infrastructure located in low-lying coastal regions, with these impacts having the potential to extend beyond the directly impacted area. It is beneficial to evaluate potential tsunami impacts on infrastructure to inform efforts to improve coastal communities' resilience to tsunami hazards.

Categories of critical infrastructure typically include distributed networks such as electricity, water, and telecommunications. These networks comprise various components distributed over a large geographical area, making risk assessments for the entire network a more complicated exercise than for spatially concentrated assets such as hospitals. Electricity distribution networks are among these distributed infrastructure networks, consisting of sub-transmission and distribution lines, substations, and transformers, which supply electricity to users in each distribution region. Although the electricity network is of vital importance to post-tsunami response, the network and its components are also vulnerable to damage from tsunamis (Williams et al., 2019, 2020). Recent tsunamis in Chile (2010), Japan (2011), Palu (2018), and Tonga (2022) damaged coastal generation and transmission facilities, disrupting the national or local electricity network (Norio et al., 2011; Mori and Takahashi, 2012; Suppasri et al., 2012; Horspool and Fraser, 2016; Omira et al., 2019; Paulik et al., 2019; WorldBank, 2022). In addition, damage to utility poles was reported following the 2004 Indian Ocean tsunami (Tang et al., 2006; Reese et al., 2007) and the 2018 Sulawesi Earthquake and Tsunami (Paulik et al., 2019). Prevalent damage modes recorded in surveys following these events included scour around pole foundations, tilted poles, poles snapped at their base and displaced poles. Even if generation assets are less vulnerable to tsunamis, damage to low-lying assets within the distribution network is likely to cause localised blackouts even under a rapid recovery scenario (Horspool and Fraser, 2016).

Risk modelling with regard to hazard impacts on infrastructure is a complex process involving several stages (Johnson and Priest, 2008). A comprehensive risk model can be developed using a number of methods, commonly involving a hazard model, asset data of the specific infrastructure being investigated, and a vulnerability model connecting the hazard to the asset. Quantification of asset vulnerability typically relies on available field data or a suitable combination of physical and numerical modelling to link a characteristic hazard magnitude scale to estimated damage levels (Koshimura et al., 2009; Suppasri et al., 2011; Macabuag et al., 2016; Alam et al., 2018b; Williams et al., 2020). Since the nearshore properties of tsunamis are strongly dependent on local features such as the offshore and nearshore bathymetry, the coastline shape and the inland topography (Yeh et al., 1989, 2005; FEMA, 2011), well-resolved numerical modelling is required to correctly capture the spatial distribution of the hazard to coastal assets. This hazard is typically expressed as the height of the tsunami bore at a given location, where the bore is characterised by a quasi-steady flow with an approximately uniform depth over a long wavelength behind a turbulent front (Hibberd and Peregrine, 1979). More recent design guidance gives consideration to hydrostatic and hydrodynamic loading (including debris impacts), considering loading cases at times of maximum inundation depth and flow velocity, respectively (ASCE, 2017). Given the availability of datasets describing the geospatial distribution of infrastructural assets, detailed information about component-level vulnerability is required to assess risk to the infrastructure – that is the focus of the work here.

This research quantifies the component-level vulnerability of utility poles under tsunami attack, providing data for a risk model of the New Zealand electricity network. The methodology and data developed here can be used to inform risk models of similar distributed infrastructure systems under threat from tsunamis and other extreme hydrodynamic events, and are generalisable beyond the New Zealand context. A series of appropriately scaled laboratory experiments were used to identify the relationship between tsunami properties and the hydrodynamic forces exerted on different utility pole geometries and orientations. The forces and inundation depths measured from the experiments were scaled and applied in nonlinear structural models that account for soil structure interaction of the embedded pole components. Results from the numerical analysis provided quantitative information on lateral pole response and damage accounting for uncertainties in bore characteristics and soil conditions. These data were compiled to perform a limit state analysis for varying pole damage levels as a function of tsunami bore height and ultimately to develop fragility functions that can be used to estimate damage.

2 Flume testing

Tsunami loads on free-standing structures have been extensively investigated using scaled flume experiments (Nouri et al., 2010; Al-Faesly et al., 2012; Shafiei et al., 2016, 2018; Arnason et al., 2009; Foster et al., 2017; Wüthrich et al., 2020). The experiments in this work were conducted at a 1:24 geometric scale in a flume where the tsunami bore was approximated as a dam-break flow generated by the sudden release of water from an upstream reservoir, where sudden was defined relative to the criteria discussed in previous research (Lauber and Hager, 1998; von Häfen et al., 2019). The dam break approach was used here because it is impractical to model tsunamis from source through propagation to runup and impact for the purpose of force generation. Previous research has used solitary waves, which has a strong theoretical underpinning as well as a "mass displacement" element that made them more useful than regular (linear) waves (Madsen et al., 2008). However, the period of these solitary waves is far too short for them to be used for tsunami load research. A dam break is currently the most widely used method for creating a bore that is representative of a tsunami as it runs up onshore (Chanson, 2006; Esteban et al., 2020; Nouri et al., 2010; Palermo et al., 2009; Wüthrich et al., 2018, 2019). Dam-break simulated tsunamis do not capture situations where a tsunami is trough-led or has any kind of complicated phasing. In addition, the simplified approach used here does not capture processes such as the receding wave of the tsunami or the increase in density through the bore's sediment load or entrained debris. However, the initial stage and steady stage of the tsunami is effectively simulated, and the rise, peak, and steady stage forces on the utility poles are captured.

Figure 1 shows side views of the flume, which is 19.2 m long and 1.2 m wide. The reservoir length is relatively short in the along-flume direction; the effects of this are discussed in prior work (Barranco and Liu, 2021). For each bore case in the experiments, the reservoir was filled to a given level, and the automatic gate was opened a set height and remained open for ten seconds before closing. The generated bore propagated down the working section of the flume before impacting the scale utility pole specimen 13.2 m from the gate of the reservoir. Each test was conducted on a dry flume bed. It should be noted that fresh water was used in the physical experiments, which created an additional density-related scaling term when applying the experimental results to the numerical model in Section 4.4 to reflect the density of salt water. It is important to note that salt-water may influence processes linked to surface tension, including debris accumulation and air-entrainment, which were not assessed in this research.
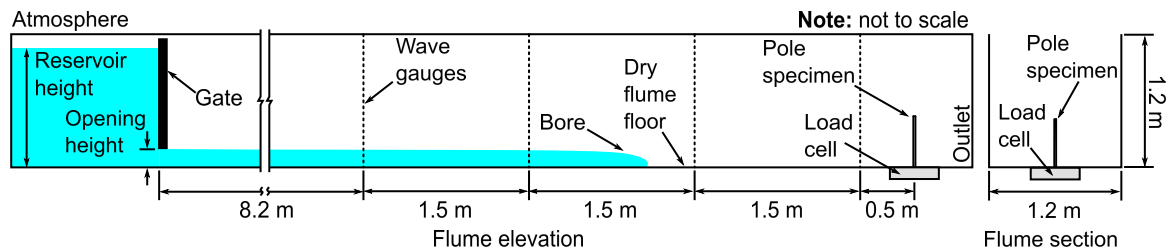

Figure 1: Experimental set-up.

2.1 Physical models and materials

The testing used three representative utility pole geometries: two I-sections representing pretensioned concrete utility poles with lengths of 11 m and 9.5 m in prototype, and a slender cylinder representing a wooden utility pole. These poles were selected as prototypes because they are commonly used in electrical distribution lines in New Zealand. Sectional dimensions of the concrete poles for both the full-scale prototype and scaled specimens are provided in Figure 2. The wooden poles at prototype had a length above the ground level 9 m and a diameter of 0.3 m, and the scale specimens had a length of 375 mm and diameter of 12 mm. All of the scale specimens were fabricated using aluminium to ensure that they withstood the hydrodynamic forces during testing. There was no coupling between structural response and the flow due to the rigidity of the aluminium models, and the experiments did not include secondary features that may impact upon the structural performance, such as cross-beams, cables and transformers. The inclusion of these features could be the focus of future research, although very small secondary features would be more subject to scale effects in the laboratory experiments. The I-section poles were tested in two configurations: one with the web facing the tsunami bore and one with the flange facing the tsunami bore. Herein this is referred to as down line and across line loading respectively as indicated in Figure 2.

2.2 Instrumentation

An initial series of experiments without the scale specimens in place were used to characterise the bore properties generated from a range of gate and reservoir conditions. Four capacitance-type wave gauges were placed at the center of the flume along its length to measure the depth of the flow and to determine the average bore tip propagation speed using a simple time-of-flight approach. The first wave gauge (WG1) was placed 8.2 m downstream from the gate, with other gauges (WG2 to WG4) equally spaced 1.5 m along the flow direction (Figure 1). The recorded time at which the bore reached each wave gauge was used to calculate the bore tip propagation speed (time of flight approach). The time of first non-zero reading at each wave gauge was taken as the time of arrival of the bore as has been done in previous work (Shafiei et al., 2016; Xu et al., 2020, 2021). The last wave gauge (WG4), together with a side-looking Nortec Vectrino acoustic Doppler velocimeter (ADV) 40 mm above the flume bed, were placed 12.7 m downstream of the gate along the centreline of the flume, Bore depths were recorded at a frequency of 1000 Hz and velocities were recorded at 200 Hz simultaneously. Five repetitions of each size of bore were conducted to obtain consistent and reliable average results under each test condition. The measured free surface elevations and bore velocities were highly repeatable, with relative errors of recorded depth from each of the repetitions within 4% and relative errors of recorded velocity within 10%. The characteristic bore heights were used as an indicator of tsunami intensity when estimating response and damage to the utility poles in the numerical analyses. To avoid any interference with the measured forces, wave gauges were removed from the flume before undertaking tests on the scale models.

During testing, each scale specimen was connected to a three-axis load cell (JR3) beneath the flume level with a base plate, ensuring that the utility pole base was located at the same elevation as floor of the flume noting that this boundary condition is not consistent with what would typically used in service where the poles are embedded in soil. The load cell provided three-axis measurements of the forces and moments exerted on the scale specimen utility poles during testing. The stream-wise force (herein referred to as base-shear) and base overturning moment are most relevant to the current study. Each of the bore impact tests was repeated three times.
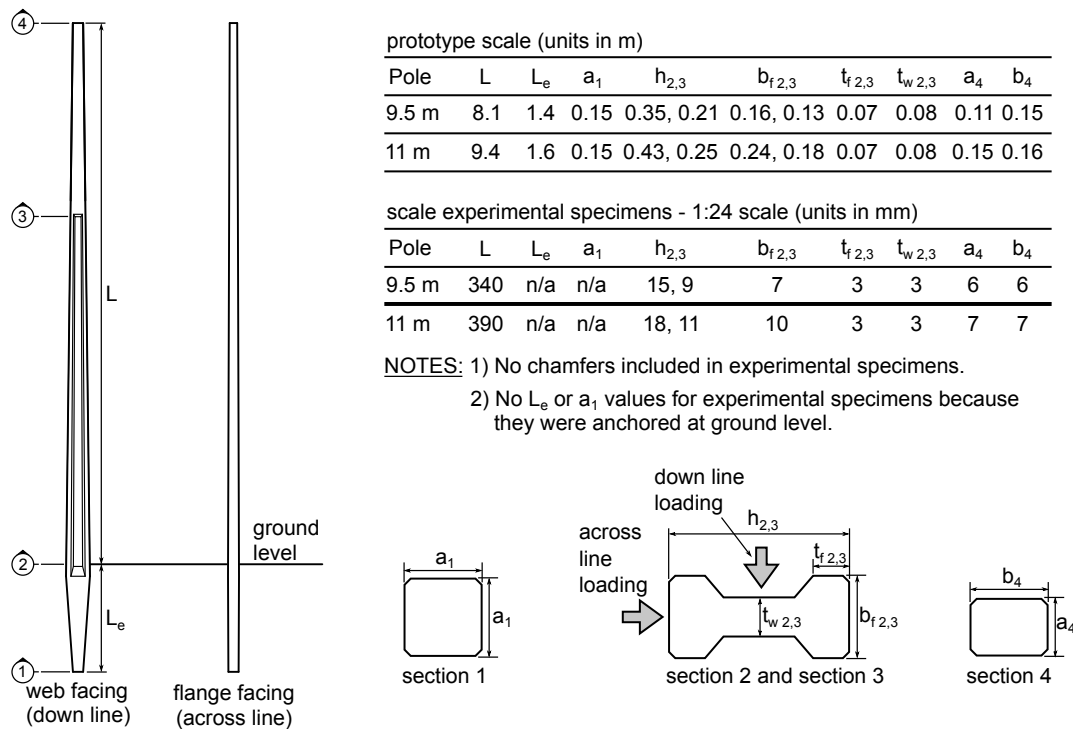

prototype scale (units in m)

Pole	L	L_e	a_1	$h_{2,3}$	$b_{f2,3}$	$t_{f2,3}$	$t_{w2,3}$	a_4	b_4
9.5 m	8.1	1.4	0.15	0.35, 0.21	0.16, 0.13	0.07	0.08	0.11	0.15
11 m	9.4	1.6	0.15	0.43, 0.25	0.24, 0.18	0.07	0.08	0.15	0.16

scale experimental specimens - 1:24 scale (units in mm)

Pole	L	L_e	a_1	$h_{2,3}$	$b_{f2,3}$	$t_{f2,3}$	$t_{w2,3}$	a_4	b_4
9.5 m	340	n/a	n/a	15, 9	7	3	3	6	6
11 m	390	n/a	n/a	18, 11	10	3	3	7	7

NOTES: 1) No chamfers included in experimental specimens.

2) No L_e or a_1 values for experimental specimens because they were anchored at ground level.

Figure 2: Concrete I-section prototype and scale models.

3 Experimental results

3.1 Bore height and velocity characteristics

Table 1 summarises the bore properties measured a distance 12.7 m downstream from the gate (0.5 m upstream from the specimen location), while Figures 3a and 3b show time series of the bore depths and velocities of selected cases (cases a, b, c, f in Table 1) at that location. In all cases, the bore was characterised by a bore front with a rapid increase in free surface elevation, followed by a quasi-steady period, which sustained for approximately five seconds. The model wave half-period $T/2$ exceeded 25 seconds for all bore cases, equivalent to a field-scale tsunami $T/2 > 158$ seconds where T is the period of the tsunami which represents the amount of time required for one cycle. Although this is relatively short compared to reported tsunami periods in the literature, the physical experiments were able to capture peak forces and moments during the quasi-steady period, hence increasing the period of the bore (using a longer gate opening time) would not lead to increased forces during testing. To fit the temporal dependence of the bore tip propagation speed and the velocities measured by the ADV, a second-order polynomial curve was used, as shown in Figure 3b (Park et al., 2013; Xu et al., 2020). The bore had a larger velocity at its front and a steady decreasing trend. The decreasing behaviour of velocities behind the front was shown in a number of previous studies, including the work of Arnason et al. (2009) for dam-break waves, Leng and Chanson (2016) for positive surges and Wüthrich et al. (2018) for tsunamis. The latter study also showed a relatively constant velocity profile across the flow depth. Figures 3c and 3d illustrate the time series of Froude number Fr and specific momentum flux hu^2. The Froude number was calculated according to Equation 1, where u is the depth-averaged velocity, h is the water depth and g is gravitational acceleration.

$$Fr = \frac{u}{\sqrt{g \times h}} \tag{1}$$

The initial experiments without the scale specimens in place showed that velocities measured at 40 mm, 80 mm and 120 mm above the flume bed were approximately equal. Therefore, velocities measured at 40 mm above the flume bed were used to calculate Fr and specific momentum flux hu^2. Fr ranges from 1.49-1.6 in the quasi-steady period for bore cases a-f in Table 1. Comparing Figures 3a and 3d, it is clear the specific momentum flux reached its maximum only slightly before the bore reached its maximum depth, indicating that bore height can be used as reasonable hazard intensity measure.

Table 1: Properties of generated tsunami bores.

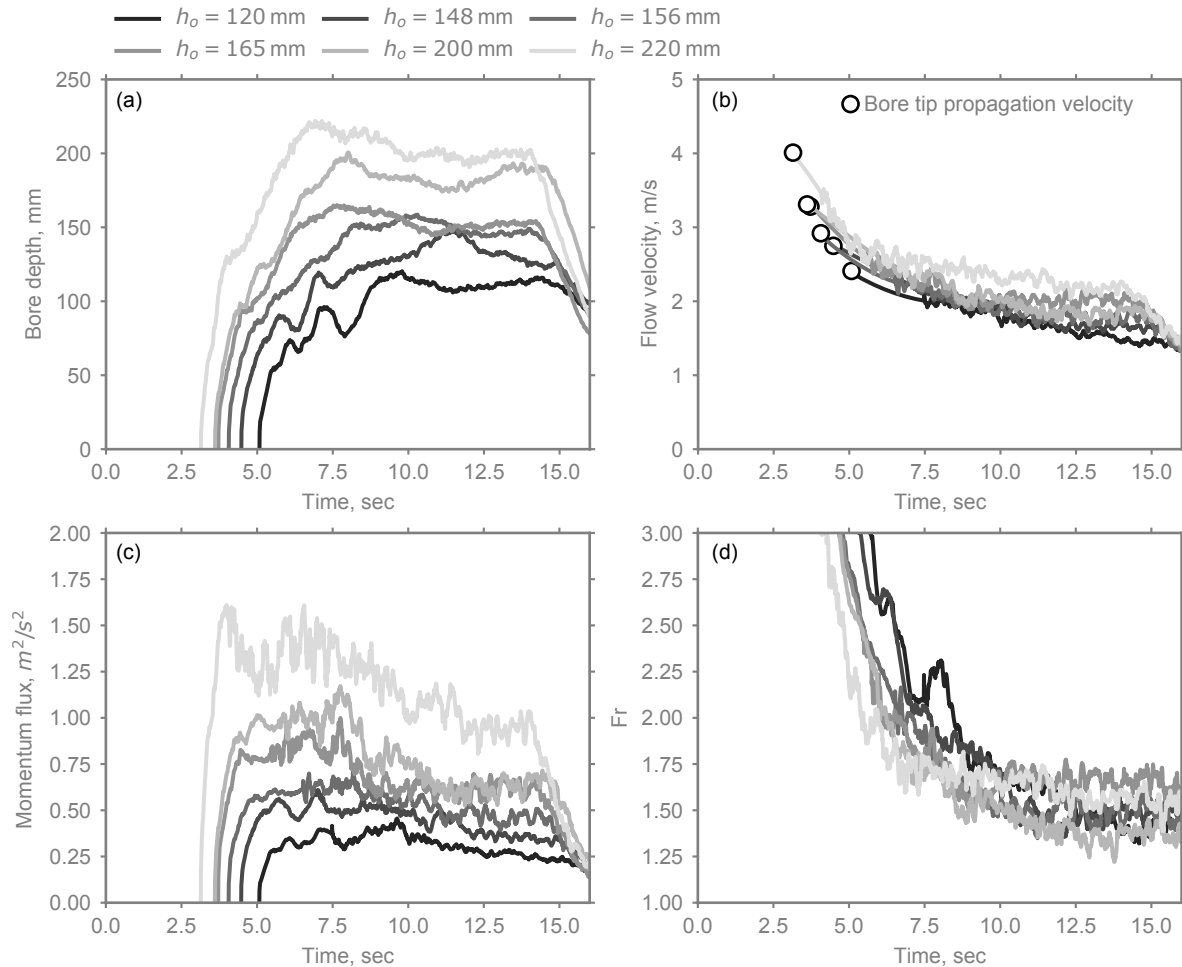| Bore cases	Reservoir water depth H, mm	Gate opening height GO, mm	Gate opening time, sec.	Maximum bore depth h_o, mm	Bore tip propagation speed U, m/s	Average Fr in the quasi-steady period
a	400	200	10	120	2.41	1.49
b	500	200	10	148	2.75	1.47
c	600	200	10	156	2.92	1.49
d	700	200	10	165	3.28	1.67
e	700	300	10	200	3.31	1.39
f	900	300	10	220	4.01	1.60

Figure 3: Time series of (a) bore depth h, (b) flow velocity u, (c) moment flux hu^2 and (d) Froude number Fr for bore cases b, c, d, and g in Table 1.

3.2 Observations of power pole-flow interaction

The flow pattern around the scale specimens in the quasi-steady stage (approximately seven seconds after the bore tip reached the specimens) is shown in Figure 4. Flow separation occurred at the downstream end of the poles in all cases. For the I-sections, the water sprayed upwards in both the leeside and upstream of the poles. The circular pole experienced the smallest wake area, compared to that of the rectangular shaped poles. The wake area increased in the down line orientation of the I-section, compared to the across line orientation.
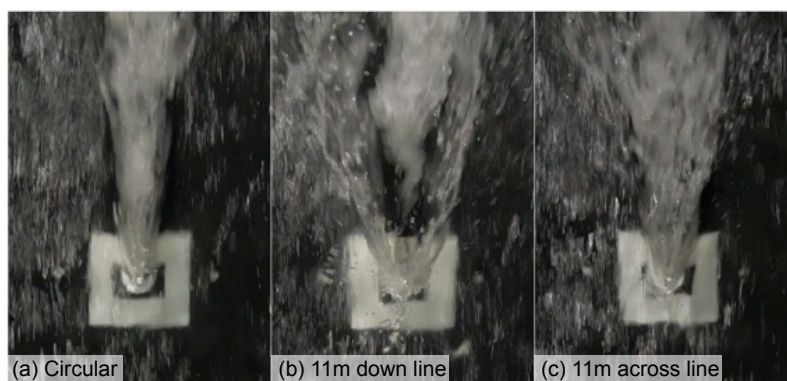

Figure 4: Flow pattern in the quasi-steady stage (7 sec after the bore tip reached specimens) for case (f) in Table 1.

3.3 Base shear and overturning moments

Figure 5 shows the time history of the horizontal base shear and overturning moments on the circular wooden pole for the six bore cases (Table 1). Unsurprisingly, the magnitude of the forces increase with increasing bore height and velocity. For the time history of overturning moments about the flume floor (Figure 5b), the trend was similar to that of the horizontal forces.

Figure 6 shows the horizontal forces on the power poles and overturning moments about the flume floor for five configurations for the largest bore case (Case (f) in Table 1). The 11 m and 9.5 m concrete poles experienced the largest force when the web faces upstream (down line loading), and the smallest force when the flange faces upstream (across line loading). A similar trend was observed for the overturning moments about the flume floor (Figure 5b and 6b).

Figure 7 illustrates the maximum forces and the maximum overturning moment about the flume floor with five pole configurations for different bore heights. Irrespective of the model shape or orientation with respect to the bore direction, the horizontal force and the overturning moment increase as the bore height increases.
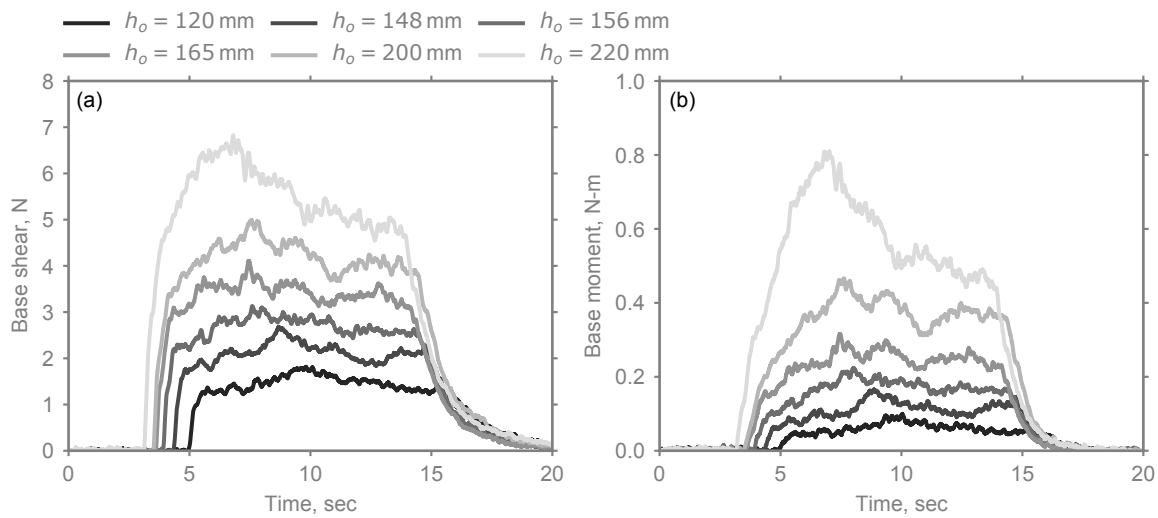

Figure 5: Time series of (a) base shear and (b) overturning moments on circular pole.
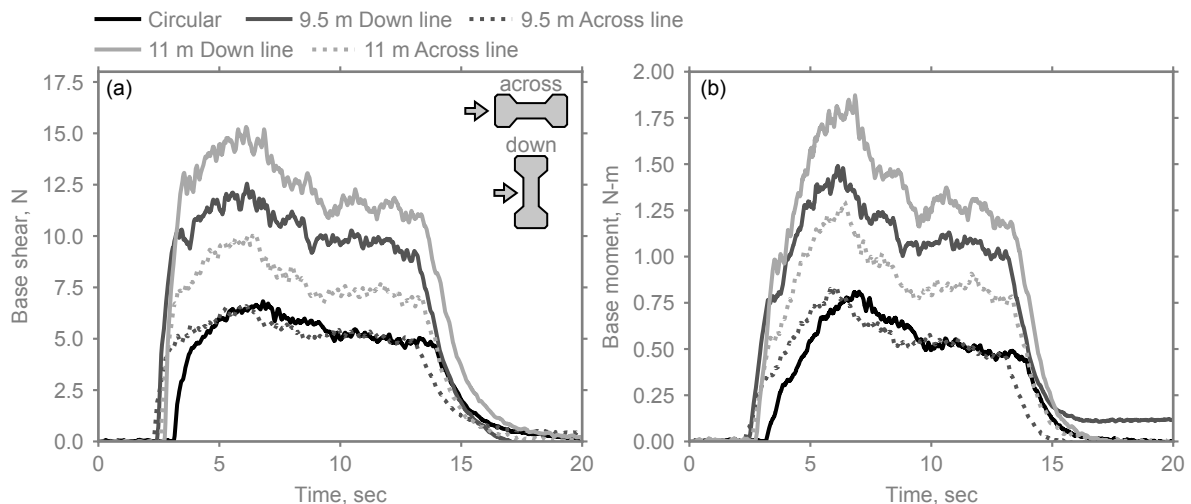

Figure 6: Time series of (a) base shear and (b) overturning moments on all pole configurations with a bore depth $h = 220$ mm.
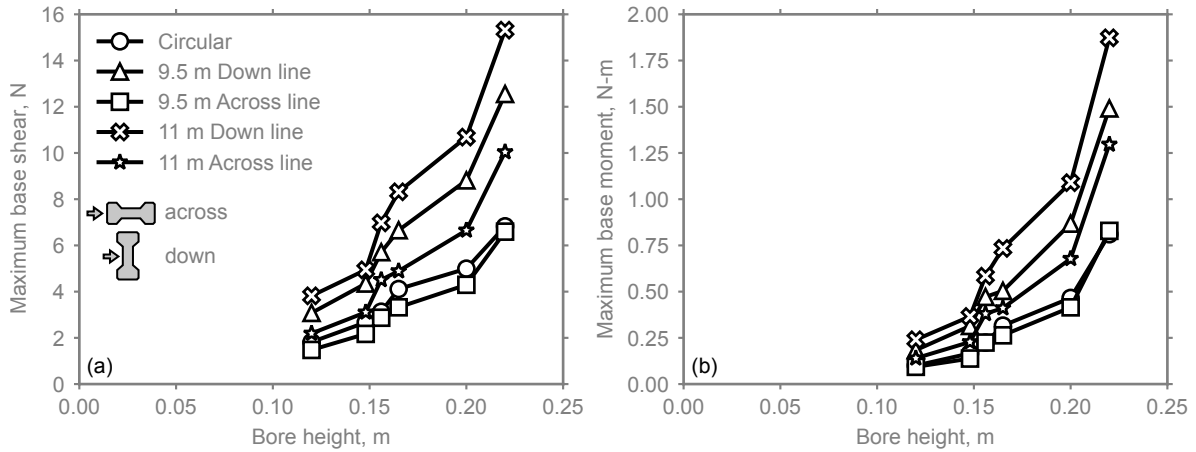
Figure 7: Maximum (a) base shear and (b) overturning moment through each loading time series relative to bore height.

3.4 Drag coefficients

Considering the hydrodynamic forces experienced by a utility pole under tsunami attack, it is interesting to consider the drag exerted on the pole by the flow. For a smooth circular cylinder in a steady flow, the drag coefficient Cd is around 1.2 for a turbulent flow characterised by a Reynolds number of $Re = 1^4 - 1 \times 10^5$ (Roshko, 1961; Cheng, 2013). For a square cylinder in the same flow conditions, Cd varies from 1.6-2.0 (Lindsey, 1938). Achenbach and Heinecke (1981) investigated the influence of the surface roughness of cylinders on Cd. A rough surface would increase Cd, especially when the Re is greater than 2×10^4. In a steady open channel flow, Cd is usually 1.8-2.2 for square cylinders and 0.78-1.15 for circular cylinders in subcritical flows (Tseng et al., 2000; Arnason et al., 2009). Cd tends to decrease with an increasing Froude number Fr when Fr is greater than 0.7 (Cassan et al., 2014; Ducrocq et al., 2017).

The drag coefficient Cd for all bore heights and pole orientations was calculated using Equation 2 where F_x is the horizontal base shear applied on the power pole, ρ is the density of the water, taken as 1000 kg/m^3, u is the depth-averaged velocity of the flow without the power pole and A is the projection area of the power pole in the direction of the flow. The projection area was calculated with the width of the submerged power pole and the water depth without the structure, assuming that the water pile-up was not significant in front of the slender structure. The Reynolds number Re for each case was calculated using Equation 3 where D is the characteristic length of the power pole and ν is the kinematic viscosity (1.0×10^6 when the water temperature is 20 °C). Figure 8a shows the time series of Cd for the five pole configurations. Cd was fairly consistent for the I-shaped poles, reaching 1.2-1.6 after the bore front. The circular pole had a smaller Cd, equal to 0.6-0.8 after the bore front.

$$Cd = \frac{2 \times F_x}{\rho \times u^2 \times A} \tag{2}$$

$$Re = \frac{u \times D}{\nu} \tag{3}$$

Given the fluctuations of Cd in the quasi-steady stage of the flow, the average Cd was taken in the quasi-steady stage for analysis. Figure 8b shows the average Cd against average Re in the quasi-steady stage of the flow (for a duration of 4 s). For the circular power pole, Cd ranges from 0.78-0.98 ($Re = 20000 - 30000$). For the rectangular concrete power poles, Cd ranges from 1.15-1.63 ($Re = 10000 - 35000$). ASCE (2017) recommended a Cd of 1.25 for rectilinear structures with a width to inundation depth ratio $b/h < 12$, where b is the width of the structure perpendicular to the flow direction and h is the inundation depth. For structural components, Cd was suggested to be 1.2-2.0. Arnason et al. (2009) reported Cd in a range of 0.78-1.15 for a circular column in subcritical flows around slender cylinders from previous steady open channel study. Cd is 0.74-0.91 for a cylindrical rod perpendicular to flow with a length to diameter ratio $L/D = 5 - 20$ ($Re = 8.8 \times 10^4$), where L is the length of the rod and D is the diameter (Blevins, 1984). Hoerner (1965) reported a Cd of 0.77 for a surface piercing circular cylinder in flow with a Froude number of 1.5. The Cd values reported in the present study

were generally consistent with previous research, although the values obtained in the current study tended to be slightly higher than the value of 1.25 provided within ASCE (2017). This value of $Cd = 1.25$ does not account for the increase in Cd with increasing Re at lower Re values evident in Figure 8b; further investigations into Reynolds number effects, particularly considering modifications to the fluid density due to suspended sediment (and debris) and scale effects may be interesting (since Re similarity is not preserved when scaling experimental results according to Fr). However, the results indicate that the Cd values do exhibit Re independence at higher Re values, despite some scatter in the data. Hence, the use of average values for relatively high Re values should suffice for design purposes. The variation of Cd with Fr in the quasi-steady stage is plotted in Figure 8c. Although the trend of Cd with Fr was not obvious in this study, particularly given the narrow range of Froude numbers tested, various other researchers showed that Cd decreases with an increasing Fr for supercritical flow (Cassan et al., 2014; Ducrocq et al., 2017). The use of representative Cd values over a range of tsunami characteristics, hence Fr values, appears to be appropriate, although users may wish to opt for a conservative (i.e. high) Cd value for design purposes.
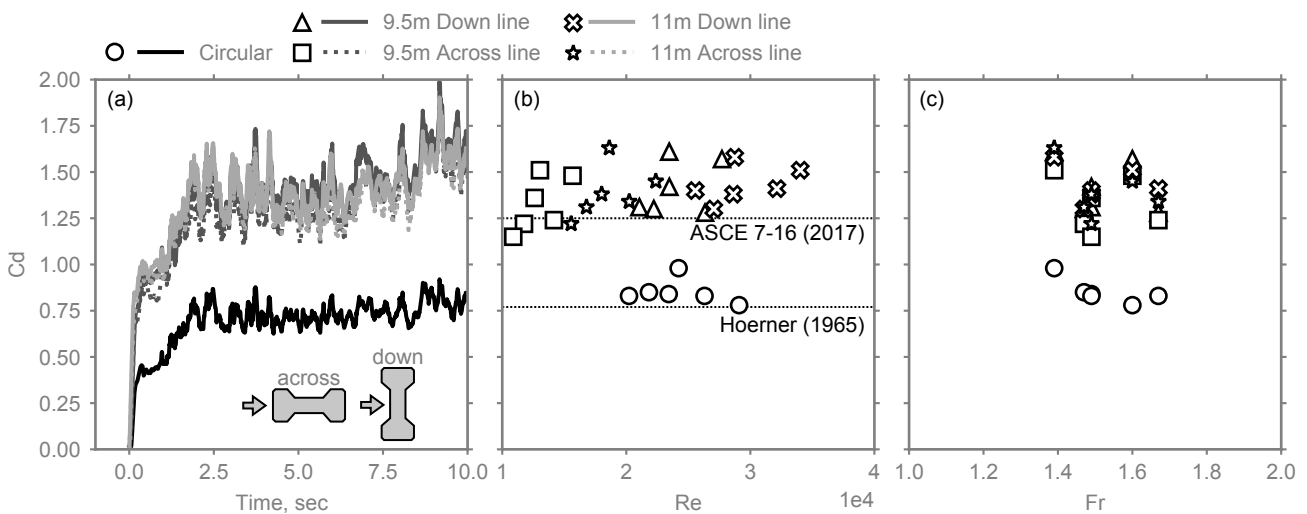

Figure 8: (a) Time history of Cd for five pole configurations with $h = 220$ mm, (b) Cd with Re in the quasi steady stage and (c) Cd with Fr in the quasi-steady stage. The Froude number Fr used in the quasi steady stage is the 4 sec-averaged value in the quasi-steady stage, which occurred at approximately 10-14 sec as shown in Figure 3c.

4 Numerical modelling

4.1 Model overview

To evaluate the response of full scale prestressed concrete utility poles subjected to tsunami bore impacts, the opensource structural analysis software OpenSeesPy (Zhu et al., 2018) was used to develop nonlinear numerical models at the prototype scale accounting for the effects of soil deformability and soil-structure interaction. The 11 m and 9.5 m prototype poles were the focus of the numerical study due to their prevalence in low-lying coastal regions in many nations in the Pacific.

An overview of the numerical model is shown in Figure 9. The utility poles were modelled using a centreline approach based on displacement based distributed plasticity beam column elements with three integration points per element. Element lengths above the ground surface were approximately 0.45 m, resulting in 20 and 18 elements for the 11 m and 9.5 m pole respectively. The length of the elements below the soil surface were 0.2 m in all cases regardless of the embedment depth L_e. Embedment depths of 1.75 m, 2.25 m, and 2.75 m were evaluated for the 11 m pole, while L_e of 1.5 m, 2.0 m, and 2.5 m were evaluated for the 9.5 m pole where 1.75 m and 1.5 m are approximately representative of embedment depths used in practice for the 11 m and 9.5 m poles respectively. A fibre based approach was used to model the pole cross sections, with an extremely fine fibre discretisation as is illustrated in Figure 9c. A total of six median cross sections were used to capture the taper in the poles, as it is not possible to explicitly model tapered sections in OpenSeesPy. Mass corresponding to the tributary length of the cross section was lumped to the nodes between the elements using a concrete density of 2400 kg/m^3.
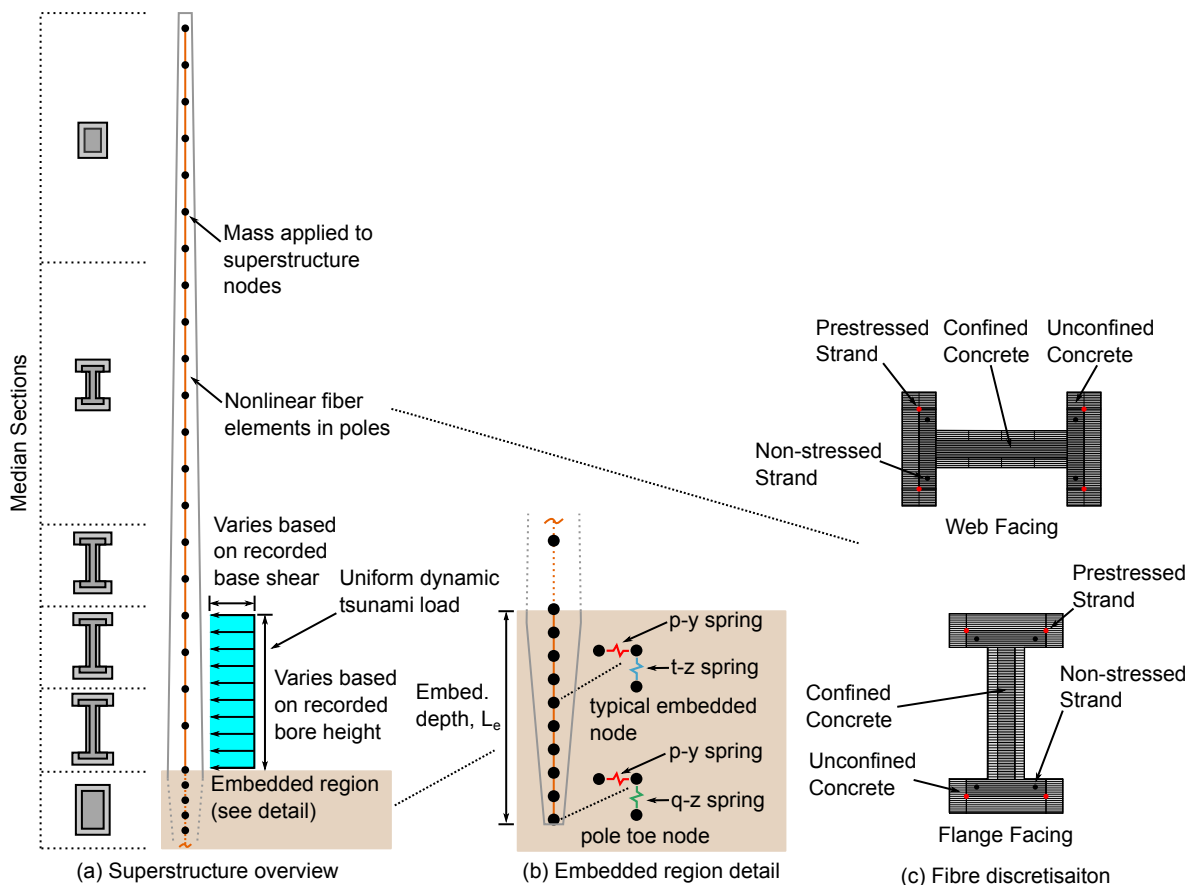

Figure 9: Schematic representation of OpenSeesPy numerical model.

4.2 Structural material modelling

Concrete and steel nonlinearity in the power poles was modelled using constitutive relationships available in OpenSeesPy. Unconfined and confined concrete was modelled using the Popovics (1973) material model with de-

graded linear unloading/reloading stiffness and exponential tensile strength decay (Concrete04 in OpenSeesPy). The confined and unconfined concrete properties are summarised in Table 2, with the confined properties calculated using the Mander (Mander et al., 1988) confinement model. The characteristic compression strength (f'_c) was based on manufacturer testing data. The stressed and unstressed strands were modelled using a Giuffre-Menegotto-Pinto (Filippou et al., 1983) material model with isotropic hardening (Steel02 in OpenSeesPy). The yield and ultimate strengths of the strand material are summarised in Table 2 and were selected based on expected in-situ strengths. Prestressing was applied to stressed strands by applying an initial strain to the steel material. Strand prestress forces of 111 kN and 101 kN were applied to strands in the 11 m and 9.5 m poles respectively. This resulted in pretensioning stresses typically used in pretensionned concrete power poles.

Table 2: OpenSeesPy material definitions.

Fibre region	Unconfined concrete	Confined concrete	Prestressing strand
Description	Popovics (1973) model	Popovics (1973) model	Giuffre-Menegotto-Pinto model (Filippou et al., 1983)
OpenSeesPy material model	Concrete04	Concrete04	Steel02
Compression/yield strength, MPa	$f'_c = 57.66$	$f'_{cc} = 69.28$	$f_y = 1770.16$
Strain at compression/yield	$\epsilon_c = 0.003$	$\epsilon_{cc} = 0.006$	n/a
Ultimate strain	$\epsilon_{cu} = 0.006$	$\epsilon_{cu} = 0.025$	n/a
Elastic modulus, MPa	$E_c = 35689$	$E_c = 35689$	$E_s = 193053$
Additional information	Tension: - $f_t = 0.1f'_c$ - $\epsilon_t = 0.001$	Tension: - $f_t = 0.1f'_c$ - $\epsilon_t = 0.001$ Confined parameters calculated using Mander et al. (1988) confinement model.	- Hardening: $b = 0.02$ - Default plastic-elastic transition parameters - Initial stress used to apply prestressing

4.3 Soil spring modelling

Soil-structure interaction in the embedded region of the pole was modelled using nonlinear $p - y$, $t - z$, and $q - z$ springs. $P - y$ springs were used to capture the lateral displacement response of the soil and consist of elastic, plastic, and gap components in series (Boulanger et al., 1999). The gap component consists of a nonlinear closure spring in parallel with nonlinear drag springs that account for soil drag around the sides of the pole. $T - z$ and $q - z$ springs were used to capture skin friction in the vertical direction and vertical bearing at the pole toe respectively. $P - y$, $t - z$, and $q - z$ springs are defined based on the ultimate soil capacity (p_{ult}, t_{ult} and q_{ult} respectively) and the displacement at 50% mobilisation of the ultimate capacity ($y50$ and $z50$) which were calculated using the undrained shear strength or friction angle for cohesive soils (clays) and cohesionless soils (sands) respectively. Cohesive soils were modelled using recommendations from Reese and Welch (1975) for $p - y$ springs and Reese and O'Neill (1987) for $t - z$ and $q - z$ springs. The recommended $y50$, $z50$ and $z50$ values were defined based on the embedded pole dimensions and values from Matlock (1970). Cohesionless soils were modelled using recommendations from API (2007) for $p - y$ springs and Mosher (1984) for $t - z$ and $q - z$ springs. The calculated properties were distributed to the soil springs based on depth and tributary length between the nodes in the embedded region. Due to the relatively shallow embedment of the poles, only a single soil layer definition with a consistent undrained shear strength (for cohesive soils) or friction angle (for cohesionless soils) was used across the entire embedded depth of the pole. The undrained shear strengths and friction angles evaluated here are summarised in Table 3 and were selected based on common soil properties in New Zealand (AS/NZS:7000:2016, 2016).

Table 3: Soil properties used to define springs for cohesive and cohesionless soils.

Cohesive soils		Cohesionless soils	
Unit weight, kN/m^3	Undrained shear strength c_u, kPa	Unit weight, kN/m^3	Friction angle ϕ, degrees
18.5	20	16	21
19.25	37.5	18	27.5
20.0	75	18	29
21.5	150	20	33
21.5	200	21	38

4.4 Loading

As shown in Figure 9, tsunami loading was applied as a dynamic uniformly distributed load (UDL) using scaled data from the experiments where the inundation depths, base shears and overturning moments were scaled using factors of 24, $24^3 \times 1.025$, and $24^4 \times 1.025$ respectively. The 1.025 factor was applied to account for fresh (rather than salt) water used in the experiments. At each time step throughout the loading history, the height of the UDL was defined based on the scaled inundation depth, while the magnitude was defined based on the scaled base shear.

The UDL approximation was verified using two approaches. First, data from the flume experiments was used to calculate the distance from the base of the poles to the location of the total resultant tsunami force, which defined the moment arm about the fixed base of the specimens. Figure 10a illustrates the normalised moment arm for the I-section pole configurations for loading Case f in Table 1 as calculated using data recorded from the experiments. For all pole configurations and geometries, there was a surge in the normalised moment arm due to water splash up at initial impact, however in the quasi-steady flow stage the normalised moment arm stabilised to 0.5 - 0.6 of the water depth which is consistent with a UDL as is indicated in the figure. Similar normalised moment arm values were observed for all bore heights. Next, the overturning moments recorded from a fixed-base model were compared to the scaled overturning moments from the experiments. For demonstration, Figure 10b shows the scaled experimental and numerical overturning moments for a 9.5 m pole loaded across line for loading cases (a), (c) and (f) from Table 1. From Figure 10b, it is clear the the numerical overturning moment histories approximately trace the experimental histories with some variation. To quantify differences in the maximum magnitudes of the experimental and numerical overturning moments, the ratios of the maximum moments (M_{exp}/M_{num}) were calculated and are summarised in Table 4 for all scaled experimental load cases, pole geometries and loading configurations. From Table 4, it is clear the numerical loading approach captured the maximum moment demands within approximately 20% in all cases.

As only six tsunami loading cases were available from the experiments for each pole type and orientation, additional loading cases were generated using bore height to base shear scale factors that were developed using a best-fit regression that related the prototype-scale bore height to the maximum recorded base shear as illustrated in Figure 11. It is worth noting that the best-fit regressions for all loading cases predict slightly un-conservative base shear values for tsunami bore heights in the range of approximately 3.75 m to 4.5 m (with the largest discrepancy occurring in the 11 m pole loaded down line). This can result in potentially un-conservative damage estimates for tsunami inundation depths in this range.

Table 4: Ratio of maximum scaled experimental overturning moment (M_{exp}) to maximum overturning moment acheived using the UDL loading approximation in the numerical model (M_{num}) - M_{exp}/M_{num}.

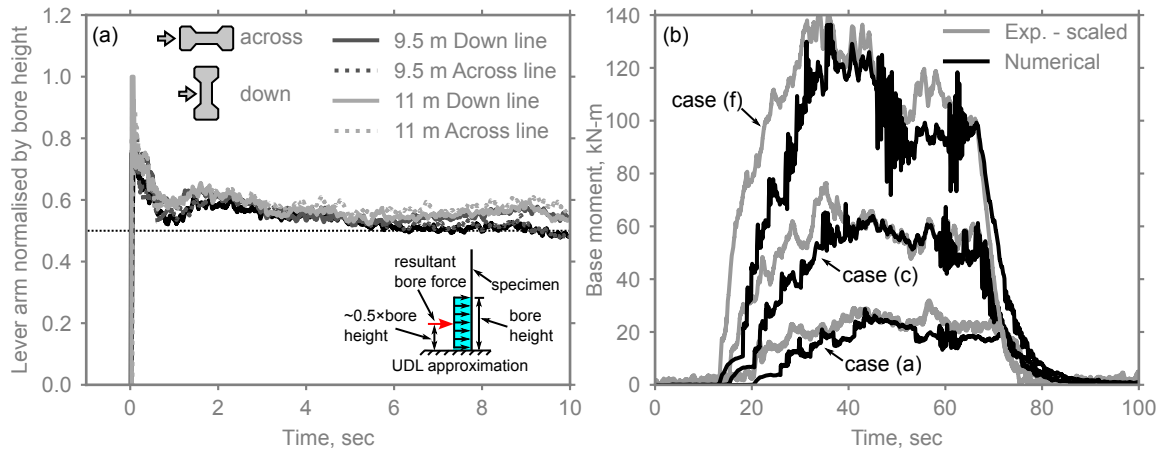|	Load cases from Table 1					
Pole and loading	(a)	(b)	(c)	(d)	(e)	(f)
9.5 m Down line	0.99	1.09	1.18	1.00	1.13	1.03
9.5 m Across line	1.10	1.05	1.11	1.04	1.03	1.13
11 m Down line	1.06	1.15	1.20	1.15	1.07	1.16
11 m Across line	0.98	1.16	1.23	1.06	1.06	1.05

Figure 10: (a) Time history of normalised moment arms for I-sections as calculated using experimental data and (b) scaled experimental and numerical overturning moments for 9.5 m across line for load cases (a), (c) and (f) in Table 1.
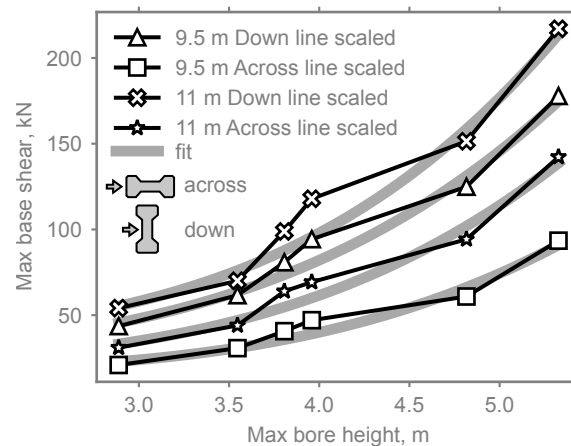

Figure 11: Maximum scaled experimental base shears and corresponding bore heights and best-fit regressions used to develop additional loading cases for the numerical analysis.

4.5 Validation

Fixed based models were developed to validate the structural modelling approach. The fixed based models were subjected to monotonic loading at the tip of the pole, and the response was compared to force-displacement data provided by the manufacturer. The models were able to effectively capture the force-displacement response through failure for the 9.5 m and 11 m poles loaded in both the down line and across line directions. The force-displacement curves cannot be included here due to proprietary restrictions however the percent difference in the maximum experimental and numerical loads prior to failure were as follows: 9.5 m pole down line – 0.9%, 9.5 m pole across line – 7.3%, 11 m pole down line – -3.8%, and 11 m pole across line – -1.4%.

5 Performance evaluation and collapse probability accounting for uncertainty in soil parameters

The pole models were subjected to tsunami loading in both the down line and across line orientations for a range of soil properties, embedment depths, and tsunami bore heights. The soil properties and pole embedment depth were selected as the primary parameters of study based on the results of a preliminary parametric evaluation that demonstrated that the structural parameters of the poles (e.g. f'_c, f_y, prestressing force) had very limited influence on the lateral response within the expected ranges of those parameters.

The models were subjected to an incremental dynamic tsunami analysis which consisted of scaling the tsunami bore loading histories until a maximum tip drift $\theta = \Delta/L$ of 25% was obtained, where Δ and L are the tip displacement and pole height from the ground surface respectively. Specifically, incrementally increasing maximum bore depths of 0.1 m were applied to the models beginning at a maximum bore depth of 0.5 m using the regression relationships shown in Figure 11. For example. in the first run a scale factor was applied to the full tsunami loading history such that the maximum bore depth was 0.5 m, in the second run a scale factor was applied to the full tsunami loading history such that the maximum bore depth was 0.6 m, and this was repeated until the tsunami loading resulted in a maximum drift θ that exceeded the limit of 25%. As an example, maximum bore height vs. maximum recorded drift plots for the 11 m pole loaded down line are shown in Figure 12, where the *healthy*, *critical*, and *unhealthy* limit states will be discussed below. Note that this scaling procedure is very similar to incremental dynamic analyses commonly used to quantify structural performance in performance based earthquake engineering applications (Vamvatsikos and Cornell, 2002).
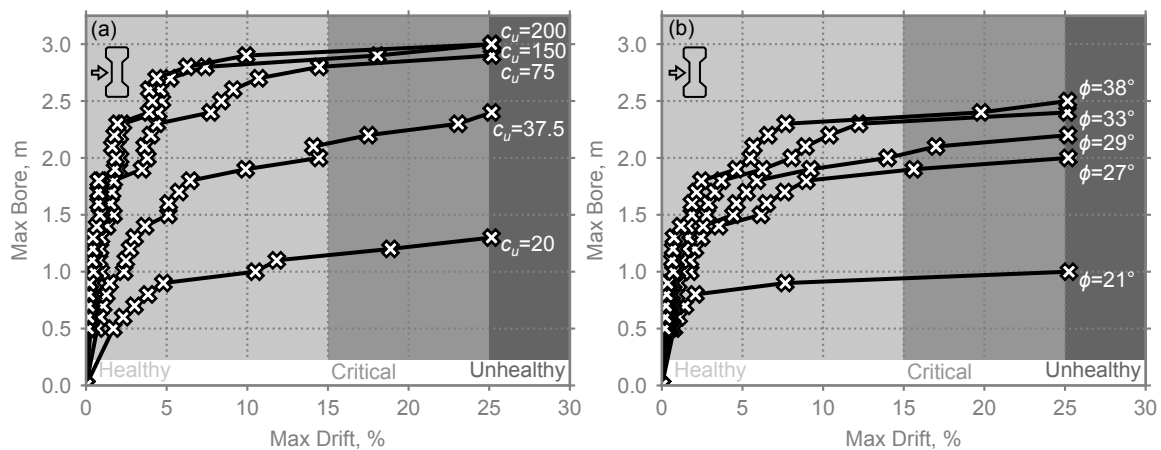

Figure 12: Relationship between maximum bore height and maximum drift for an 11 m pole loaded in the down line direction with an embedment depth $L_e = 2.75$ m in (a) cohesive soils with undrained shear strengths in kPa and (b) cohesionless soils.

5.1 Failure modes

The failure mode of the poles was characterised by either rigid body pole rotation or pole hinging below the soil surface depending on the stiffness of the soil, the embedment depth of the pole, and the orientation of loading (across or down line). Figures 13 and 14 show the deformed shape of an 11 m pole loaded down line at 25% drift (as measured from the ground surface) after being subjected to a tsunami with a 4.75 m bore height for cohesive and cohesionless soils respectively. The 4.75 m bore case was selected for demonstration because this resulted in drifts in excess of 25% for all embedment depths and soil stiffnesses for this pole. From Figures 13 and 14, it is clear that the embedment depth and soil stiffness directly influence the observed failure mode. As illustrated in Figure 13, the failure mode of the 11 m pole in cohesive soils loaded down line with an embedment depth of 1.75 m (commonly used embedment in practice) was characterised by rigid body rotation for a soil with an undrained shear strength of 75 kPa, while pole hinging was observed for an undrained shear strength of 200 kPa. When the embedment depth was increased to 2.75 m, pole hinging was observed for all undrained shear strengths. Similarly for cohesionless soils, larger soil stiffness and embedment depths resulted in failures characterised by pole hinging rather than rigid body rotation as shown in Figure 14. It is important to note, however, that for cohesionless soils the embedment depth played a much larger role than the soil stiffness in shifting the failure mode towards pole hinging. When comparing failure modes in cohesive and cohesionless soils in cases where pole hinging developed, the location of the hinge was generally deeper in cohesionless soils as is demonstrated in Figures Figures 13d and 14d. Similar trends in failure modes were observed for all pole geometries and soils characteristics.
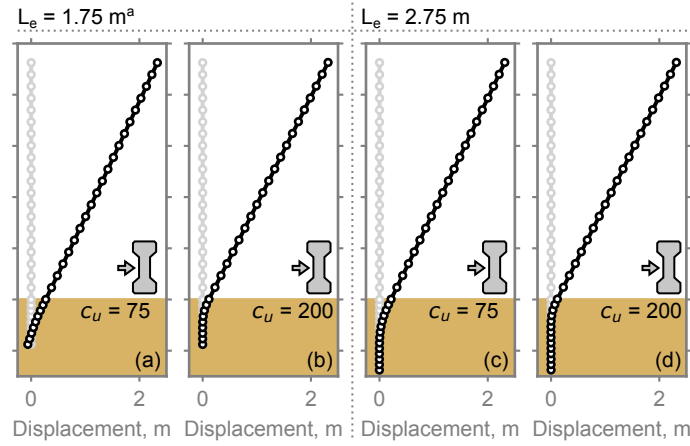
Figure 13: Deformed shape at 25% drift of 11 m pole anchored in cohesive soil with a range of undrained shear strengths resulting from a 4.75 m tsunami bore loaded down line. [a]indicates typical embedment used in practice and undrained shear strengths are in kPa.
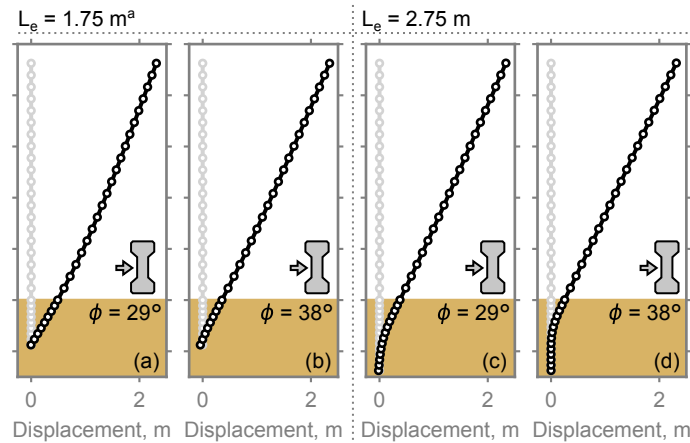

Figure 14: Deformed shape at 25% drift of 11 m pole anchored in cohesionless soil with a range of friction angles resulting from a 4.75 m tsunami bore loaded down line. [a]indicates typical embedment used in practice.

To provide a basis for estimating the failure mode as a function of the provided embedment depth and soil stiffness, the theoretical active and rigid embedment lengths were calculated for all soil stiffnesses and pole geometries evaluated here. The active length L_a is defined in Equation 4 (Gazetas, 1991) where E_p and E_s are the elastic moduli of the pole and soil respectively and D is the equivalent circular diameter, while the rigid length L_r is defined in Equation 5 (Carter and Kulhawy, 1992) where the variable definitions are the same. The active length is commonly used to characterise the behaviour of long piles and describes the region over which pile deformation occurs within the embedded region, whereas the rigid length is used to characterise the behaviour of short piles where rigid body rotation is expected for embedment depths less than the rigid length. A simplified approach was used here, with the elastic soil conditions used to define these parameters.

$$L_a = 2.0 \times D_1 \times \left(\frac{E_p}{E_{so}} \right)^{0.26} \tag{4}$$

$$L_r = 0.07 \times D_1 \times \left(\frac{E_p}{E_{so}} \right)^{0.5} \tag{5}$$

Figures 15 and 16 show the ratio of the active and rigid lengths to the provided embedment depths (L_e/L_a depth and L_e/L_r) as a function of the ratio of the maximum observed moment to theoretical plastic moment capacity of the poles. In these figures, $M_{max}/M_p > 1$ indicates a pole hinging failure mode while $M_{max}/M_p < 1$ indicates rigid body rotation failure mode. From Figure 15, it is clear that both the active and rigid lengths can be used to estimate failure modes of poles embedded in cohesive soils, where the active length is a slightly

more conservative indicator. As shown in Figure 15a, when considering the active length pole hinging was achieved for all L_e/L_a values greater than 0.8, whereas when considering the rigid length pole hinging was only observed for L_e/L_r values greater than 1.0 (as shown in Figure 15b). For poles embedded in cohesionless soils, only the active length appears to provide a reasonable indicator for the expected failure mode. As shown in Figure 16a, when considering the active length pole hinging was generally achieved for L_e/L_a values greater than 1.0. Conversely when considering the rigid length, M_{max}/M_p values of less than 1.0 were observed for Lr/Le values of up to 1.5 (as shown in Figure 16b).

Figure 15: Relationship between maximum pole moment recorded below soil surface and (a) theoretical active length and (b) theoretical rigid length for poles embedded in cohesive soils subjected to a 4.75 m tsunami bore.
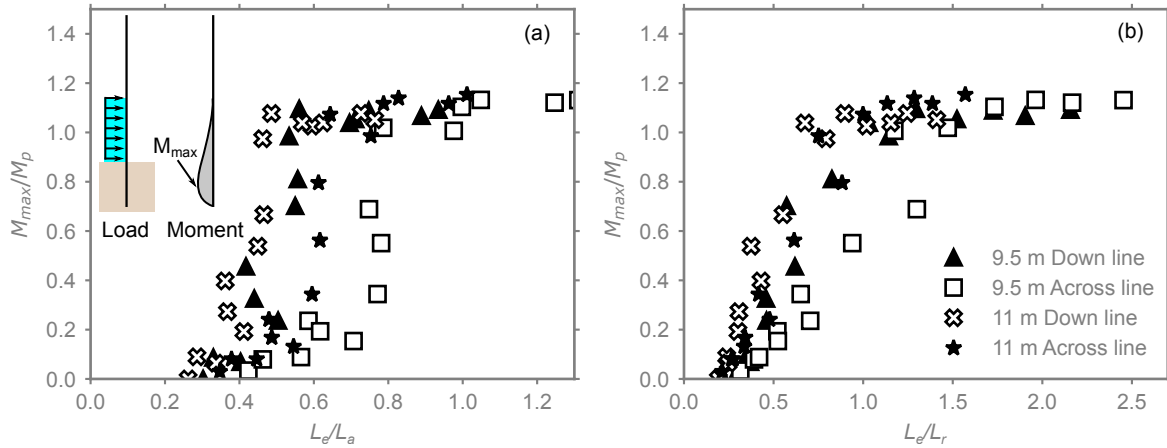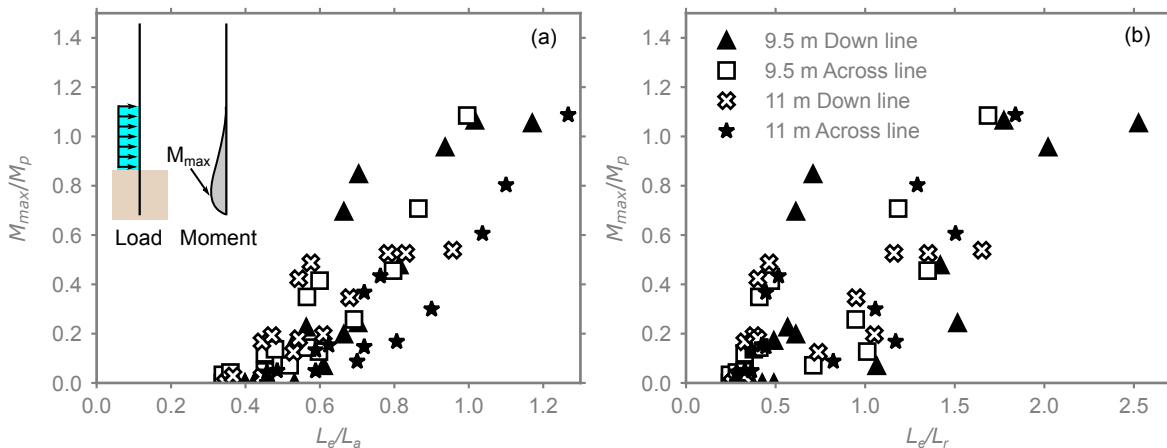

Figure 16: Relationship between maximum pole moment recorded below soil surface and (a) theoretical active length and (b) theoretical rigid length for poles embedded in cohesionless soils subjected to a 4.75 m tsunami bore.

5.2   Limit state evaluation

The performance of the poles was evaluated using three limit states representing *healthy*, *critical*, and *unhealthy* pole conditions as defined by Alam et al. (2018a) for utility poles subjected to hurricane loading. These limit states estimate pole condition based on the tip drift where LS1 - *healthy* is $0 \leq \theta < 0.15$, LS2 - *critical* is $0.15 \leq \theta < 0.25$, and LS3 – *unhealthy* is $\theta \geq 0.25$. Note that only the bore depths resulting in maximum drifts exceeding the unhealthy limit state are presented here, because in all cases the difference in bore depths needed to exceed the critical and unhealthy limit state were relatively small (0.1-0.2 m) as is illustrated in Figure 12 for the 11 m pole loaded down line. This is due to significant inelastic deformation and stiffness degradation in the poles and/or soil at the critical limit state of 15%, which results in large increases in drift with small increases in demand beyond that point. This is demonstrated by the small shallow slopes in the curves across the critical limit state in Figure 12. These results indicate that future testing could use larger laboratory models to reduce the geometrical scale factor, focusing on smaller prototype-scale tsunami bore heights. This would

allow refinement of the limit states determined herein, and avoid the vast majority of laboratory-scale bores being large enough to immediately lead to *unhealthy* limit states.

The maximum bore depths required to exceed the *unhealthy* limit state are shown in Figures 17 and 18 for poles embedded in cohesive and cohesionless soils respectively. For both the cohesive and cohesionless cases, the soil stiffness, embedment depth, and orientation of loading significantly influenced the maximum bore depth to exceed the *unhealthy* limit state. Considering the 9.5 m pole embedded in cohesive soils as an example (Figure 17a and 17b) it is clear that the soil stiffness played the largest role in the maximum bore depth at the *unhealthy* limit state for poles in cohesive soils. When loaded down line, a maximum bore depth of 2.5 m resulted in pole hinging, which developed for larger undrained shear strengths (greater than 75 kPa) as shown in Figure 17a. When loaded across line, larger soil stiffnesses (greater than 150 kPa) were required to develop pole hinging which occurred at a bore depth of 4.5 m as shown in Figure 17b. In cases of softer soil where failure was dominated by rigid body rotation, the maximum bore depths to exceed the *unhealthy* limit state ranged from 0.6 m-2.4 m and 0.6 m-4.4 m for loading down line and across line respectively depending on the pole embedment depth and soil stiffness.

Considering the 9.5 m pole embedded in cohesionless soils as an example, it is clear that both the pole embedment depth and the soil stiffness play a significant role in the maximum bore depth at the *unhealthy* limit state for poles in cohesionless soils. When loaded down line, a maximum bore depth of 2.1 m resulted in pole hinging, which only developed for large embedment depths and large soil stiffnesses. For down line loading, hinging only developed in poles with the maximum embedment depth of 2.5 m for soils with friction angles of 27.5°, 29°, and 33°as shown in Figure 18a; for a friction angle of 38°hinging developed for embedment depths of both 2.0 m and 2.5 m. This phenomenon is exacerbated when looking at across line loading, where hinging developed at a maximum bore depth of 4.2 m which was only observed for the maximum embedment depth of 2.5 m and maximum friction angle of 38 as shown in Figure 18b. In the cases of softer soils, maximum bore depths as low as 0.5 m resulted in drifts that exceeded the *unhealthy* limit state.
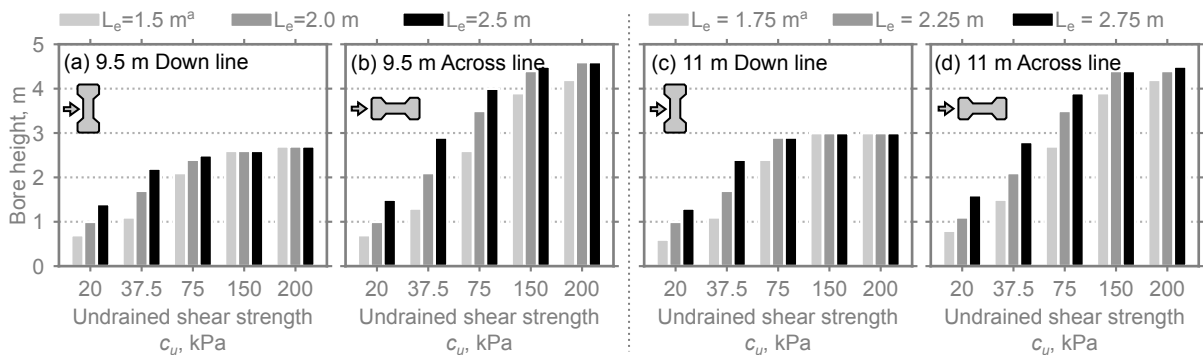

Figure 17: *Unhealthy* limit-state bore height for poles embedded in cohesive soil. [a] indicates typical embedment used in practice.

Figure 18: *Unhealthy* limit-state bore height for poles embedded in cohesionless soil. [a] indicates typical embedment used in practice.

One interesting note when comparing the same pole geometry and loading orientation for poles embedded in cohesive and cohesionless soils is the different maximum bore depth that results in pole hinging at the *unhealthy* limit state. As an example, when considering the 9.5 m pole loaded down line (Figure 17a and 18a for cohesive

and cohesionless soils respectively), the maximum bore depth that results in pole hinging is 2.5 m for cohesive soils and 2.1 m respectively. This is due to the location of the hinge below the soil surface – hinging in the cohesionless soil develops at a larger depth which results in a larger moment arm between the location of the resultant tsunami force and hinge location. An example of this can be seen in Figure 13 and Figure 14 for an 11 m pole loaded downline.

It is important to note that the fragility functions presented here do not account for soil scour, which would undoubtedly influence the expected performance of the poles. The effective embedment depth of the poles would decrease with increasing levels of scour, which would decrease expected bore heights that would exceed the *unhealthy* limit state.

5.3 Collapse probability accounting for soil uncertainty

Results from the incremental dynamic tsunami analysis were used to fit lognormal cumulative distribution functions (CDFs) that estimate the probability that the *unhealthy* limit state will be exceeded given a tsunami bore depth. The CDFs were fit using the procedure described in Baker (2015), where median (θ_m) and dispersion (β) values were selected to minimize bias between the empirical data and the closed form solution. The dispersion values calculated for the CDFs presented here represent uncertainty in the soil stiffness which directly influences the failure mode (rigid body rotation or pole hinging). The range of soil parameters used to generate the CDFs are consistent with the range presented in Table 3.

The fitted closed form CDFs for the *unhealthy* limit state are shown in Figures 19 and 20 for poles embedded in cohesive and cohesionless soils respectively, while the fitted constants (θ_m and β) are given in Table 5. Poles with lower embedment depths tended to have larger dispersion values due to increased uncertainty in the failure mode, which resulted in intersecting CDFs in several instances (e.g. in Figure 19a, the CDF for an embedment depth of 1.5 m intersects the CDFs for embedment depths of 2.0 and 2.5 m). In these cases, the curve generated for the largest embedment depth was set as the limit at which all other CDFs were cutoff, as this curve typically represented a pole hinging (or close to pole hinging) failure mode as indicated in Figures 17 and 18. At the point of pole hinging, it is not physically possible to resist a larger bore depth before failure.

From Figures 19 and 20, it is clear that increasing the embedment depth can significantly improve the probabilistic performance of the poles in both cohesive and cohesionless soils, although the improvement in performance in cohesionless soils is more significant. Taking the 9.5 m pole loaded across line as an example, the median bore depth to exceed the unhealthy limit state (e.g. the bore depth with a probability of exceedance of 50%) increased from 1.67 m to 2.60 m for poles in cohesive soils and 0.91 m to 2.81 m for poles in cohesionless soils as shown in Figures 19b and 20b and Table 4 when the embedment depth was increased from 1.5 m (the embedment typically used in practice) to 2.5 m. Similar increases in performance were observed for all poles for all loading orientations.

Table 5: Median (θ_m) and dispersion (β) for the fitted fragility functions in Figures 19 and 20.

Cohesive soils (Figure 19)								
	9.5 m Across line		9.5 m Down line		11 m Across line		11 m Down line	
Embed., m[a]	θ_m	β	θ_m	β	θ_m	β	θ_m	β
1.5/1.75	1.34	0.78	1.67	1.00	1.42	1.03	1.87	0.87
2.0/2.25	1.87	0.39	2.49	0.68	2.13	0.90	2.68	1.06
2.5/2.75	1.91	0.37	2.60	0.65	2.41	0.73	3.11	0.41
Cohesionless soils (Figure 20)								
1.5/1.75	0.50	2.14	0.91	1.49	0.60	2.02	1.00	1.82
2.0/2.25	0.93	2.09	1.61	1.93	1.08	2.08	1.83	1.73
2.5/2.75	1.41	1.51	2.81	1.48	1.57	1.71	3.00	1.14

Figure 19: *Unhealthy* limit-state fragility functions for poles embedded in cohesive soil. [a] indicates typical embedment used in practice.

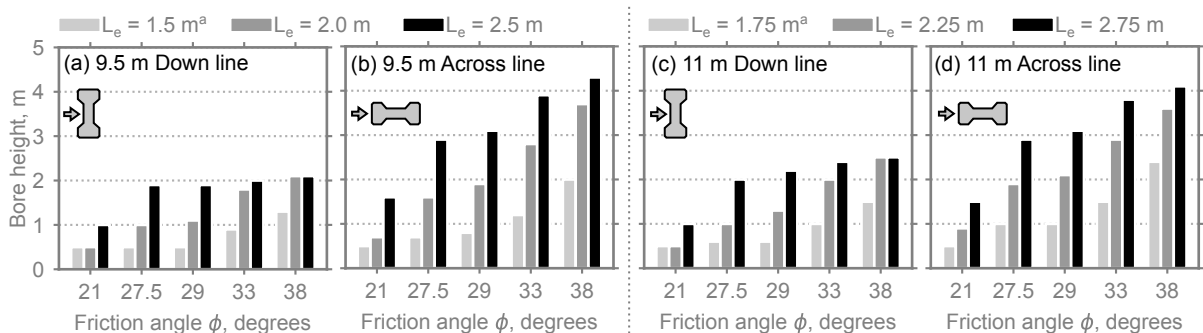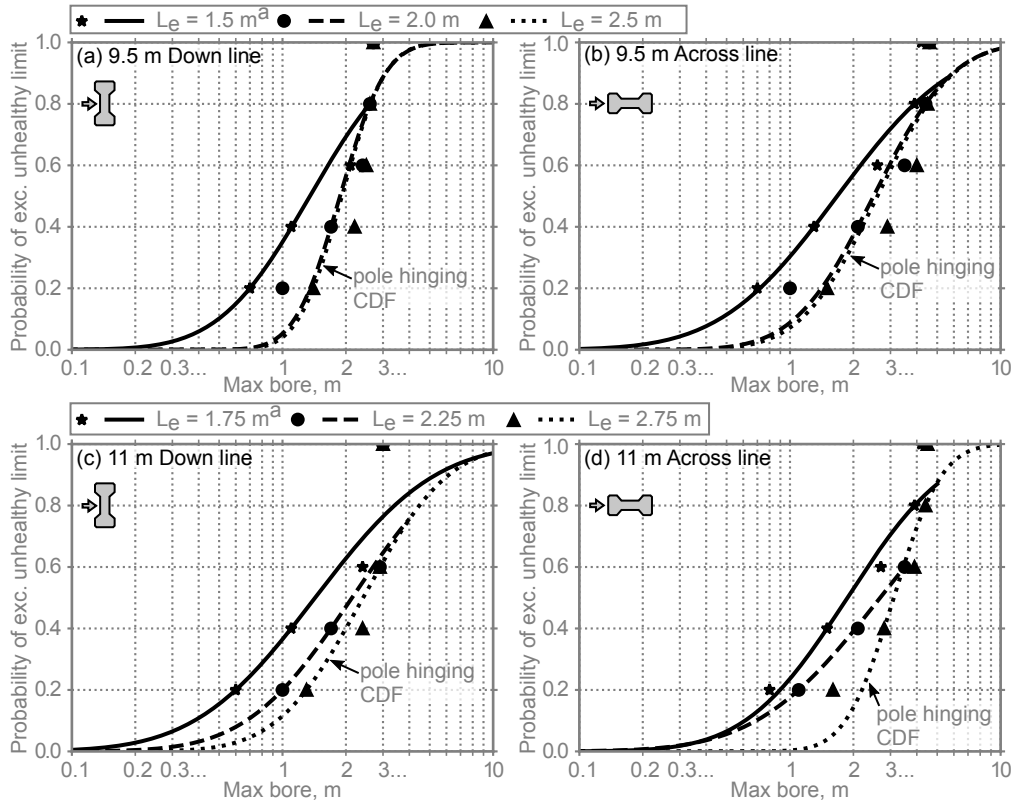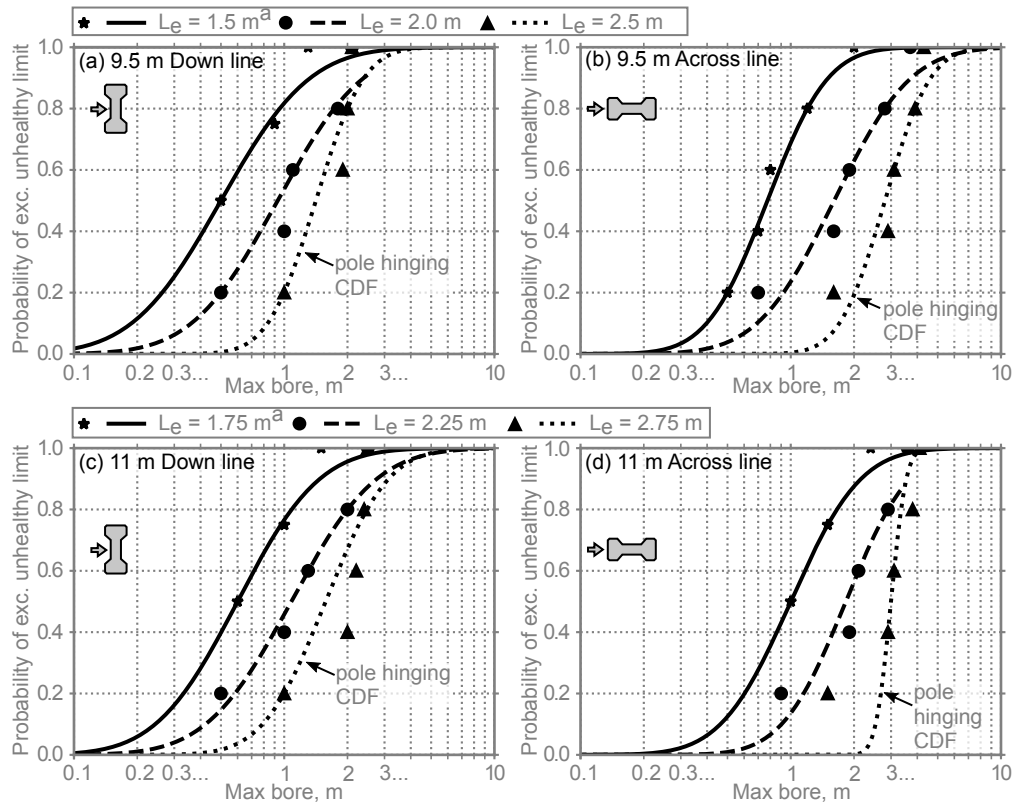
Figure 20: *Unhealthy* limit-state fragility functions for poles embedded in cohesionless soil. [a] indicates typical embedment used in practice.

6 Summary and conclusions

Tsunami limit state and fragility data were generated for common distribution line utility poles in New Zealand using scaled flume experiments and nonlinear numerical modelling. The flume experiments were used to explore relationships between wave properties and important flow parameters and to generate hydrodynamic loading histories on different utility pole geometries and orientations. Nonlinear numerical models that account for soil structure interaction were developed and validated using experimental data. The loading histories from the flume tests were scaled and used in the numerical models to perform an incremental dynamic tsunami analysis. Results from that analysis were used to investigate failure modes and generate probabilistic tools that can be used estimate damage to utility poles subjected to tsunami attack. The following conclusions are drawn from the work.

- The orientation of the 9.5 m and 11 m utility poles (down line or across line) played an important role in determining the base shear and overturning moment during tsunami attack.

- The drag coefficients measured within these experiments were slightly higher than those reported in previous research, although the data exhibited considerable scatter in their dependence on both Reynolds number and Froude number.

- The soil characteristics play a significant role in the response of utility poles subjected to tsunami loading. Poles embedded in stiffer soils tended to exhibit a pole hinging failure mode and larger tsunami bore depths before exceeding the unhealthy limit state than poles embedded in softer soils.

- Increasing the embedment depth can significantly improve the response of utility poles embedded in softer soils. Providing an embedment depth 1m larger than the manufacturer specified embedment tended to shift the failure mode from rigid body rotation towards pole hinging for both the 9.5 m and 11 m poles.

- The active and rigid length concepts that are commonly used to characterise the behaviour of laterally loaded piles can be used to estimate the failure mode of power distribution poles subjected to tsunami attack. For poles embedded in cohesive soils, both techniques provided conservative estimates of failure mode, while for poles embedded in cohesionless soils the active length technique was shown to be effective.

- The limit state and probabilistic tools developed here can be used in power distribution network models to assist in evaluating network-wide disruptions resulting from tsunamis impacts on low-lying power distribution assets.

- Flume experiments should be guided by preliminary numerical structural analysis, to determine an appropriate range of prototype-scale tsunami bore heights. This would help to avoid an excessively large geometric scale factor, which in turn increases the likelihood that most (or all) of the model-scale bore heights would lead to structural failure.

- To enable a more complete understanding of the tsunami vulnerability of distributed power infrastructure, more detailed analyses should be conducted accounting for additional uncertainties such as soil scour and the effects of powerlines.

Author contributions (CRediT)

MTS: Numerical modelling, visualisation, writing-original draft; ZX: Experimental testing, writing-original draft, manuscript draft review; CW: Project planning, experimental testing, manuscript draft review and editing; LW: Project planning, numerical modelling, manuscript draft review and editing

Data availability statement

Some or all data, models, and/or code that support the findings of this work are available from the corresponding author upon reasonable request.

Nomenclature

β	Dispersion in fitted cumulative distribution (fragility) functions
Δ	Displacement at the top of the utility pole
ϵ_c	Concrete strain at f_c' in unconfined concrete
ϵ_{cc}	Concrete strain at f_{cc}' in confined concrete
ϵ_{cu}	Ultimate concrete strain
ϵ_t	Concrete strain at f_t
ν	Kinematic viscosity
ϕ	Friction angle in conhesionless soils
θ	Drift angle measured from soil surface to top of utility pole
θ_m	Median value in fitted cumulative distribution (fragility) functions
A	Projection area of utility pole in the direction of flow
a_1	Width and height of utility pole cross section at Section 1 in Figure 2
a_4	Height of utility pole cross section at Section 4 in Figure 2
b	Hardening parameter for prestressing steel
b_4	Width of utility pole cross section at Section 4 in Figure 2
$b_{2,3}$	Flange width of utility poles at Sections 2 and 3 in Figure 2
c_u	Undrained shear strength of cohesive soil
Cd	Drag coefficient
D	Characteristic length of utility pole
D_1	Equivalent circular utility pole diameter
E_c	Modulus of elasticity of concrete
E_p	Equivalent modulus of elasticity of utility pole
E_s	Modulus of elasticity of steel
E_{so}	Modulus of elasticity of soil
f_c'	Compression strength of unconfined concrete

f'_y	Yield strength of prestressing strand
f'_{cc}	Compression strength of confined concrete
f_t	Tensile strength of concrete
F_x	Horizontal base shear
Fr	Froude number
g	Gravitational acceleration
H	Reservoir water depth
h	Bore depth
h_o	Maximum bore depth
$h_{2,3}$	Total cross-section height of utility poles at Sections 2 and 3 in Figure 2
hu^2	Momentum flux
L	Utility pole height above ground level
L_a	Active length of utility pole
L_e	Utility pole embedment depth in soil
L_r	Rigid length of utility pole
M_{exp}	Maximum scaled experimental overturning moment
M_{max}	Maximum utility pole moment resulting from tsunami loading
M_{num}	Maximum overturning moment achieved using UDL loading approximation in numerical model
M_p	Theoretical plastic moment capacity of the utility pole
p_u	Ultimate capacity of $p-y$ soil spring
q_u	Ultimate capacity of $q-z$ soil spring
R_e	Reynolds number
T	Period of tsunami wave
t_u	Ultimate capacity of $t-z$ soil spring
$t_{f2,3}$	Flange thickness of utility poles at Sections 2 and 3 in Figure 2
$t_{w2,3}$	Web thickness of utility poles at Sections 2 and 3 in Figure 2
U	Bore tip propagation speed
u	Depth averaged bore velocity
$y50$	Displacement at 50% mobilisation of p-y soil spring
$z50$	Displacement at 50% mobilisation of q-z and t-z soil springs

References

Achenbach, E. and Heinecke, E. (1981). On vortex shedding from smooth and rough cylinders in the range of Reynolds numbers 6×103 to 5×106. *Journal of Fluid Mechanics*, **109**, 239–251. ISSN 1469-7645, 0022-1120. DOI:10.1017/S002211208100102X. Publisher: Cambridge University Press.

Al-Faesly, T., Palermo, D., Nistor, I. and Cornett, A. (2012). Experimental Modeling of Extreme Hydrodynamic Forces on Structural Models. *International Journal of Protective Structures*, **3**(4), 477–505. ISSN 2041-4196. DOI:10.1260/2041-4196.3.4.477. Publisher: SAGE Publications.

Alam, M., Tokgoz, B.E., Safa, M. and Hwang, S. (2018*a*). Evaluation of Effects of Wind Speed on Resilience of Electric Poles, In: *IIE Annual Conference. Proceedings*, 557–562, Institute of Industrial and Systems Engineers (IISE), Norcross, United States, num Pages: 557-562.

Alam, M.S., Barbosa, A.R., Scott, M.H., Cox, D.T. and van de Lindt, J.W. (2018*b*). Development of Physics-Based Tsunami Fragility Functions Considering Structural Member Failures. *Journal of Structural Engineering*, **144**(3), 04017221. ISSN 1943-541X. DOI:10.1061/(ASCE)ST.1943-541X.0001953. Publisher: American Society of Civil Engineers.

API (2007). Recommended practice for planning, designing, and constructing fixed offshore platforms: Section 6.8 Soil Reaction for Laterally Loaded Piles.

Arnason, H., Petroff, C. and Yeh, H. (2009). Tsunami Bore Impingement onto a Vertical Column. *Journal of Disaster Research*, **4**(6), 391–403. DOI:10.20965/jdr.2009.p0391. Publisher: Fuji Technology Press Ltd.

ASCE (2017). *ASCE 7-16 Minimum Design Loads and Associated Criteria for buildings and Other Structures*, American Society of Civil Engineers, Reston VA.

AS/NZS:7000:2016 (2016). *Overhead Line Design*, Standards New Zealand, Wellington, NZ.

Baker, J.W. (2015). Efficient Analytical Fragility Function Fitting Using Dynamic Structural Analysis. *Earthquake Spectra*, **31**(1), 579–599. ISSN 8755-2930. DOI:10.1193/021113EQS025M. Publisher: SAGE Publications Ltd STM.

Barranco, I. and Liu, P.L.F. (2021). Run-up and inundation generated by non-decaying dam-break bores on a planar beach. *Journal of Fluid Mechanics*, **915**, A81. ISSN 0022-1120, 1469-7645. DOI:10.1017/jfm.2021.98. Publisher: Cambridge University Press.

Blevins, R.D. (1984). *Applied fluid dynamics handbook*, Van Nostrand Reinhold Co., New York, N.Y, open Library ID: OL3172282M.

Boulanger, R.W., Curras, C.J., Kutter, B.L., Wilson, D.W. and Abghari, A. (1999). Seismic Soil-Pile-Structure Interaction Experiments and Analyses. *Journal of Geotechnical and Geoenvironmental Engineering*, **125**(9), 750–759. ISSN 1090-0241. DOI:10.1061/(ASCE)1090-0241(1999)125:9(750). Publisher: American Society of Civil Engineers.

Carter, J.P. and Kulhawy, F.H. (1992). Analysis of Laterally Loaded Shafts in Rock. *Journal of Geotechnical Engineering*, **118**(6), 839–855. ISSN 0733-9410. DOI:10.1061/(ASCE)0733-9410(1992)118:6(839). Publisher: American Society of Civil Engineers.

Cassan, L., Tien, T.D., Courret, D., Laurens, P. and Dartus, D. (2014). Hydraulic Resistance of Emergent Macroroughness at Large Froude Numbers: Design of Nature-Like Fishpasses. *Journal of Hydraulic Engineering*, **140**(9), 04014043. ISSN 1943-7900. DOI:10.1061/(ASCE)HY.1943-7900.0000910. Publisher: American Society of Civil Engineers.

Chanson, H. (2006). Tsunami surges on dry coastal plains: Application of dam break wave equations. *Coastal Engineering Journal*, **48**(4). DOI:https://doi.org/10.1142/S0578563406001477.

Cheng, N.S. (2013). Calculation of Drag Coefficient for Arrays of Emergent Circular Cylinders with Pseudofluid Model. *Journal of Hydraulic Engineering*, **139**(6), 602–611. ISSN 1943-7900. DOI:10.1061/(ASCE)HY.1943-7900.0000722. Publisher: American Society of Civil Engineers.

De Lange, W.P. and Healy, T.R. (1986). New Zealand tsunamis 1840–1982. *New Zealand Journal of Geology and Geophysics*, **29**(1), 115–134. ISSN 0028-8306. DOI:10.1080/00288306.1986.10427527. Publisher: Taylor & Francis _eprint: https://doi.org/10.1080/00288306.1986.10427527.

De Lange, W.P. and Healy, T.R. (2001). Tsunami Hazard for the Auckland Region and Hauraki Gulf, New Zealand. *Natural Hazards*, **24**(3), 267–284. ISSN 1573-0840. DOI:10.1023/A:1012051113852.

Ducrocq, T., Cassan, L., Chorda, J. and Roux, H. (2017). Flow and drag force around a free surface piercing cylinder for environmental applications. *Environmental Fluid Mechanics*, **17**(4), 629–645. ISSN 1573-1510. DOI:10.1007/s10652-016-9505-9.

Esteban, M., Roubos, J., Iimura, K., Salet, J., Hofland, B., Bricker, J., , Ishii, H., Hamano, G., Takabatake, T. and Shibarama, T. (2020). Effect of bed roughness on tsunami bore propagation and overtopping. *Coastal Engineering*, **157**. DOI:https://doi.org/10.1016/j.coastaleng.2019.103539.

Ewing, L., Takahashi, S. and Petroff, C.M. (2013). *Tohoku, Japan, Earthquake and Tsunami of 2011*, American Society of Civil Engineers.

FEMA (2011). FEMA P-55 Coastal Construction Manual.

Filippou, F., Popov, E. and Bertero, V. (1983). Effects of bond deterioration on hysteretic behavior of reinforced concrete joints, Technical Report UCB/EERC-83/19, Earthquake Engineering Research Center.

Foster, A., Rossetto, T. and Allsop, W. (2017). An experimentally validated approach for evaluating tsunami inundation forces on rectangular buildings. *Coastal Engineering*, **128**. DOI:https://doi.org/10.1016/j.coastaleng.2017.07.006.

Foytong, P., Ruangrassamee, A., Shoji, G., Hiraki, Y. and Ezura, Y. (2013). Analysis of Tsunami Flow Velocities during the March 2011 Tohoku, Japan, Tsunami. *Earthquake Spectra*, **29**(1_suppl), 161–181. ISSN 8755-2930. DOI:10.1193/1.4000128. Publisher: SAGE Publications Ltd STM.

Fraser, S., Raby, A., Pomonis, A., Goda, K., Chian, S.C., Macabuag, J., Offord, M., Saito, K. and Sammonds, P. (2013). Tsunami damage to coastal defences and buildings in the March 11th 2011 Mw9.0 Great East Japan earthquake and tsunami. *Bulletin of Earthquake Engineering*, **11**(1), 205–239. ISSN 1573-1456. DOI:10.1007/s10518-012-9348-9.

Fritz, H.M., Phillips, D.A., Okayasu, A., Shimozono, T., Liu, H., Mohammed, F., Skanavis, V., Synolakis, C.E. and Takahashi, T. (2012). The 2011 Japan tsunami current velocity measurements from survivor videos at Kesennuma Bay using LiDAR. *Geophysical Research Letters*, **39**(7). ISSN 1944-8007. DOI:10.1029/2011GL050686. _eprint: https://onlinelibrary.wiley.com/doi/pdf/10.1029/2011GL050686.

Gazetas, G. (1991). Foundation Vibrations, In: H.Y. Fang (Editor), *Foundation Engineering Handbook*, 553–593, Springer US, Boston, MA.

Goff, J., Goto, K., Chagué, C., Watanabe, M., Gadd, P.S. and King, D.N. (2018). New Zealand's most easterly palaeotsunami deposit confirms evidence for major trans-Pacific event. *Marine Geology*, **404**, 158–173. ISSN 0025-3227. DOI:10.1016/j.margeo.2018.08.001.

Goff, J., Pearce, S., Nichol, S.L., Chagué-Goff, C., Horrocks, M. and Strotz, L. (2010). Multi-proxy records of regionally-sourced tsunamis, New Zealand. *Geomorphology*, **118**(3), 369–382. ISSN 0169-555X. DOI:10.1016/j.geomorph.2010.02.005.

Hibberd, S. and Peregrine, D.H. (1979). Surf and run-up on a beach: a uniform bore. *Journal of Fluid Mechanics*, **95**(2), 323–345. ISSN 1469-7645, 0022-1120. DOI:10.1017/S002211207900149X. Publisher: Cambridge University Press.

Hoerner, S.F. (1965). *Fluid Dynamic Drag : Practical Information on Aerodynamic Drag and Hydrodynamic Resistance*, Liselotte A. Hoerner, second edition edition.

Horspool, N. and Fraser, S. (2016). An Analysis of Tsunami Impacts to Lifelines, Technical Report 2016/22, GNS Science.

Johnson, C.L. and Priest, S.J. (2008). Flood Risk Management in England: A Changing Landscape of Risk Responsibility? *International Journal of Water Resources Development*, **24**(4), 513–525. ISSN 0790-0627. DOI: 10.1080/07900620801923146. Publisher: Routledge _eprint: https://doi.org/10.1080/07900620801923146.

Kawashima, K. and Buckle, I. (2013). Structural Performance of Bridges in the Tohoku-Oki Earthquake. *Earthquake Spectra*, **29**(1_suppl), 315–338. ISSN 8755-2930. DOI:10.1193/1.4000129. Publisher: SAGE Publications Ltd STM.

Koshimura, S., Oie, T., Yanagisawa, H. and Imamura, F. (2009). Developing Fragility Functions for Tsunami Damage Estimation Using Numerical Model and Post-Tsunami Data from Banda Aceh, Indonesia. *Coastal Engineering Journal*, **51**(3), 243–273. ISSN 2166-4250. DOI:10.1142/S0578563409002004. Publisher: Taylor & Francis _eprint: https://doi.org/10.1142/S0578563409002004.

Lauber, G. and Hager, W.H. (1998). Experiments to dambreak wave: Horizontal channel. *Journal of Hydraulic Research*, **36**(3), 291–307. ISSN 0022-1686. DOI:10.1080/00221689809498620. Publisher: Taylor & Francis _eprint: https://doi.org/10.1080/00221689809498620.

Leng, X. and Chanson, H. (2016). Coupling between free-surface fluctuations, velocity fluctuations and turbulent reynolds stresses during the upstream propagation of positive surges, bores and compression waves. *Environmental Fluid Mechanics*, **16**. DOI:https://doi.org/10.1007/s10652-015-9438-8.

Lindsey, W.F. (1938). Drag of cylinders of simple shapes, nTRS Author Affiliations: NTRS Report/Patent Number: NACA-TR-619 NTRS Document ID: 19930091694 NTRS Research Center: Legacy CDMS (CDMS).

Macabuag, J., Rossetto, T., Ioannou, I., Suppasri, A., Sugawara, D., Adriano, B., Imamura, F., Eames, I. and Koshimura, S. (2016). A proposed methodology for deriving tsunami fragility functions for buildings using optimum intensity measures. *Natural Hazards*, **84**(2), 1257–1285. ISSN 1573-0840. DOI:10.1007/s11069-016-2485-8.

Madsen, P., Fuhrman, D. and Schäffer, H. (2008). On the solitary wave paradigm for tsunamis. *Journal of Geophysical Research*, **113**(C12). DOI:https://doi.org/10.1029/2008JC004932.

Mander, J.B., Priestley, M.J.N. and Park, R. (1988). Theoretical Stress-Strain Model for Confined Concrete. *Journal of Structural Engineering*, **114**(8), 1804–1826. ISSN 0733-9445. DOI:10.1061/(ASCE) 0733-9445(1988)114:8(1804). Publisher: American Society of Civil Engineers.

Matlock, H. (1970). Correlation for design of laterally loaded piles in soft clay, In: *Proceedings of the offshore technology conference*, OnePetro.

Mori, N. and Takahashi, T. (2012). Nationwide Post Event Survey and Analysis of the 2011 Tohoku Earthquake Tsunami. *Coastal Engineering Journal*, **54**(1), 1250001–1–1250001–27. ISSN 2166-4250. DOI:10.1142/S0578563412500015. Publisher: Taylor & Francis _eprint: https://doi.org/10.1142/S0578563412500015.

Mosher, R. (1984). Load-Transfer Criteria for Numerical Analysis of Axially Loaded Piles in Sand, Technical Report K-84-1, US Army Corps of Engineers.

Norio, O., Ye, T., Kajitani, Y., Shi, P. and Tatano, H. (2011). The 2011 eastern Japan great earthquake disaster: Overview and comments. *International Journal of Disaster Risk Science*, **2**(1), 34–42. ISSN 2192-6395. DOI: 10.1007/s13753-011-0004-9.

Nouri, Y., Nistor, I., Palermo, D. and Cornett, A. (2010). Experimental Investigation of Tsunami Impact on Free Standing Structures. *Coastal Engineering Journal*, **52**(1), 43–70. ISSN 2166-4250. DOI:10.1142/S0578563410002117. Publisher: Taylor & Francis _eprint: https://doi.org/10.1142/S0578563410002117.

Omira, R., Dogan, G.G., Hidayat, R., Husrin, S., Prasetya, G., Annunziato, A., Proietti, C., Probst, P., Paparo, M.A., Wronna, M., Zaytsev, A., Pronin, P., Giniyatullin, A., Putra, P.S., Hartanto, D., Ginanjar, G., Kongko, W., Pelinovsky, E. and Yalciner, A.C. (2019). The September 28th, 2018, Tsunami In Palu-Sulawesi, Indonesia: A Post-Event Field Survey. *Pure and Applied Geophysics*, **176**(4), 1379–1395. ISSN 1420-9136. DOI:10.1007/s00024-019-02145-z.

Palermo, D., Nistor, I., Nouri, Y. and Cornett, A. (2009). Tsunami loading of near-shoreline structures: a primer. *Canadian Journal of Civil Engineering*, **36**(11). DOI:https://doi.org/10.1139/L09-104.

Park, H., Cox, D.T., Lynett, P.J., Wiebe, D.M. and Shin, S. (2013). Tsunami inundation modeling in constructed environments: A physical and numerical comparison of free-surface elevation, velocity, and momentum flux. *Coastal Engineering*, **79**, 9–21. ISSN 0378-3839. DOI:10.1016/j.coastaleng.2013.04.002.

Paulik, R., Gusman, A., Williams, J.H., Pratama, G.M., Lin, S.l., Prawirabhakti, A., Sulendra, K., Zachari, M.Y., Fortuna, Z.E.D., Layuk, N.B.P. and Suwarni, N.W.I. (2019). Tsunami Hazard and Built Environment Damage Observations from Palu City after the September 28 2018 Sulawesi Earthquake and Tsunami. *Pure and Applied Geophysics*, **176**(8), 3305–3321. ISSN 1420-9136. DOI:10.1007/s00024-019-02254-9.

Popovics, S. (1973). A numerical approach to the complete stress strain curve for concrete. *Cement and Concrete Research*, **3**(5). DOI:https://doi.org/10.1016/0008-8846(73)90096-3.

Power, W., Wallace, L., Wang, X. and Reyners, M. (2012). Tsunami Hazard Posed to New Zealand by the Kermadec and Southern New Hebrides Subduction Margins: An Assessment Based on Plate Boundary Kinematics, Interseismic Coupling, and Historical Seismicity. *Pure and Applied Geophysics*, **169**(1), 1–36. ISSN 1420-9136. DOI:10.1007/s00024-011-0299-x.

Reese, L. and O'Neill, M. (1987). Drilled Shafts: ConstructionProcedures and Design Methods, Technical Report FHWA-HI-88-042, US Department of Transportation, Federal Highway Administration.

Reese, L.C. and Welch, R.C. (1975). Lateral Loading of Deep Foundations in Stiff Clay. *Journal of the Geotechnical Engineering Division*, **101**(7), 633–649. DOI:10.1061/AJGEB6.0000177. Publisher: American Society of Civil Engineers.

Reese, S., Cousins, W.J., Power, W.L., Palmer, N.G., Tejakusuma, I.G. and Nugrahadi, S. (2007). Tsunami vulnerability of buildings and people in South Java - field observations after the July 2006 Java tsunami. *Natural Hazards and Earth System Sciences*, **7**, 573–589. ISSN 1684-9981 Natural Hazards and Earth System Sciences1561-8633. DOI:10.5194/nhess-7-573-2007. ADS Bibcode: 2007NHESS...7..573R.

Roshko, A. (1961). Experiments on the flow past a circular cylinder at very high Reynolds number. *Journal of Fluid Mechanics*, **10**(3), 345–356. ISSN 1469-7645, 0022-1120. DOI:10.1017/S0022112061000950. Publisher: Cambridge University Press.

Shafiei, S., Melville, B.W. and Shamseldin, A.Y. (2016). Experimental investigation of tsunami bore impact force and pressure on a square prism. *Coastal Engineering*, **110**, 1–16. ISSN 0378-3839. DOI:10.1016/j.coastaleng.2015.12.006.

Shafiei, S., Melville, B.W. and Shamseldin, A.Y. (2018). Instant tsunami bore pressure and force on a cylindrical structure. *Journal of Hydro-environment Research*, **19**, 28–40. ISSN 1570-6443. DOI:10.1016/j.jher.2018.01.004.

Shimozono, T., Sato, S., Okayasu, A., Tajima, Y., Fritz, H.M., Liu, H. and Takagawa, T. (2012). Propagation and Inundation Characteristics of the 2011 Tohoku Tsunami on the Central Sanriku Coast. *Coastal Engineering Journal*, **54**(1), 1250004–1–1250004–17. ISSN 2166-4250. DOI:10.1142/S0578563412500040. Publisher: Taylor & Francis _eprint: https://doi.org/10.1142/S0578563412500040.

Suppasri, A., Koshimura, S., Imai, K., Mas, E., Gokon, H., Muhari, A. and Imamura, F. (2012). Damage Characteristic and Field Survey of the 2011 Great East Japan Tsunami in Miyagi Prefecture. *Coastal Engineering Journal*, **54**(1), 1250005–1–1250005–30. ISSN 2166-4250. DOI:10.1142/S0578563412500052. Publisher: Taylor & Francis _eprint: https://doi.org/10.1142/S0578563412500052.

Suppasri, A., Koshimura, S. and Imamura, F. (2011). Developing tsunami fragility curves based on the satellite remote sensing and the numerical modeling of the 2004 Indian Ocean tsunami in Thailand. *Natural Hazards and Earth System Sciences*, **11**(1), 173–189. ISSN 1561-8633. DOI:10.5194/nhess-11-173-2011. Publisher: Copernicus GmbH.

Tang, A., Ames, D., McLaughlin, J., Murugesh, G., Plant, G., Yashinsky, M., Eskijian, M., Surrampalli, R., Murthy, P.A.K., Prasad, M. and Gandhi, P. (2006). Coastal Indian Lifelines after the 2004 Great Sumatra Earthquake and Indian Ocean Tsunami. *Earthquake Spectra*, **22**(3_suppl), 607–639. ISSN 8755-2930. DOI:10.1193/1.2206089. Publisher: SAGE Publications Ltd STM.

Tseng, M.H., Yen, C.L. and Song, C.C.S. (2000). Computation of three-dimensional flow around square and circular piers. *International Journal for Numerical Methods in Fluids*, **34**(3), 207–227. ISSN 1097-0363. DOI:10.1002/1097-0363(20001015)34:3⟨207::AID-FLD31⟩3.0.CO;2-R. _eprint: https://onlinelibrary.wiley.com/doi/pdf/10.1002/1097-0363%2820001015%2934%3A3%3C207%3A%3AAID-FLD31%3E3.0.CO%3B2-R.

Vamvatsikos, D. and Cornell, C.A. (2002). Incremental dynamic analysis. *Earthquake Engineering & Structural Dynamics*, **31**(3), 491–514. ISSN 1096-9845. DOI:10.1002/eqe.141. _eprint: https://onlinelibrary.wiley.com/doi/pdf/10.1002/eqe.141.

von Häfen, H., Goseberg, N., Stolle, J. and Nistor, I. (2019). Gate-Opening Criteria for Generating Dam-Break Waves. *Journal of Hydraulic Engineering*, **145**(3), 04019002. ISSN 1943-7900. DOI:10.1061/(ASCE)HY.1943-7900.0001567. Publisher: American Society of Civil Engineers.

Williams, J.H., Paulik, R., Wilson, T.M., Wotherspoon, L., Rusdin, A. and Pratama, G.M. (2020). Tsunami Fragility Functions for Road and Utility Pole Assets Using Field Survey and Remotely Sensed Data from the 2018 Sulawesi Tsunami, Palu, Indonesia. *Pure and Applied Geophysics*, **177**(8), 3545–3562. ISSN 1420-9136. DOI:10.1007/s00024-020-02545-6.

Williams, J.H., Wilson, T.M., Horspool, N., Lane, E.M., Hughes, M.W., Davies, T., Le, L. and Scheele, F. (2019). Tsunami impact assessment: development of vulnerability matrix for critical infrastructure and application to Christchurch, New Zealand. *Natural Hazards*, **96**(3), 1167–1211. ISSN 1573-0840. DOI:10.1007/s11069-019-03603-6.

WorldBank (2022). The january 15, 2022 hunga tonga-hunga ha'apai eruption and tsunami, tonga, Technical Report Global Rapid Post Disaster Damage Estimation (GRADE) Report, World Bank and the Global Facility for Disaster Reduction and Recovery.

Wüthrich, D., Pfister, M., Nistor, I. and Schleiss, A. (2018). Experimental study of tsunami-like waves generated with a vertical release technique on dry and wet beds. *Coastal Engineering*, **144**(4). DOI:https://doi.org/10.1016/j.coastaleng.2020.103753.

Wüthrich, D., Pfister, M. and Schleiss, A. (2019). Effect of bed roughness on tsunami-like waves and induced loads on buildings. *Coastal Engineering*, **152**. DOI:https://doi.org/10.1016/j.coastaleng.2019.103508.

Wüthrich, D., Pfister, M. and Schleiss, A. (2020). Forces on buildings with openings and orientation in a steady post-tsunami free-surface flow. *Coastal Engineering*, **161**. DOI:https://doi.org/10.1016/j.coastaleng.2020.103753.

Xu, Z., Melville, B., Nandasena, N.A.K., Whittaker, C., Shamseldin, A. and Farvizi, F. (2021). Tsunami loads on slab bridges. *Coastal Engineering*, **165**. DOI:https://doi.org/10.1016/j.coastaleng.2021.103853.

Xu, Z., Melville, B.W., Wotherspoon, L. and Nandasena, N.A.K. (2020). Stability of composite breakwaters under tsunami attack. *Journal of Waterway, Port, Coastal and Ocean Engineering*, **146**(4). DOI:doi.org/10.1061/(ASCE)WW.1943-5460.0000571.

Yeh, H., Ghazali, A. and Marton, I. (1989). Experimental study of bore run-up. *Journal of Fluid Mechanics*, **206**, 563–578. ISSN 1469-7645, 0022-1120. DOI:10.1017/S0022112089002417. Publisher: Cambridge University Press.

Yeh, H., Robertson, I. and Preuss, J. (2005). Development of design guidelines for structures that serve as tsunami vertical evacuation sites, Technical Report 2005-4, Washington State Department of Natural Resources.

Zhu, M., McKenna, F. and Scott, M.H. (2018). OpenSeesPy: Python library for the OpenSees finite element framework. *SoftwareX*, **7**, 6–11. ISSN 2352-7110. DOI:10.1016/j.softx.2017.10.009.